JGR Solid Earth

RESEARCH ARTICLE
10.1029/2025JB032422

Special Collection:
Analyzing Big Data for Understanding Climate Variability, Natural Phenomena and Rapid Environmental Changes

Global Primary and Secondary Microseism Multi-Decade Geographic Variation, Secular Intensification, and Period Lengthening

Richard C. Aster[1], **Thomas A. Lee**[2], **Frederik J. Simons**[2], **Adam T. Ringler**[3], and **Robert E. Anthony**[3]

[1]Department of Geosciences and Warner College of Natural Resources, Colorado State University, Fort Collins, CO, USA, [2]Department of Geosciences, Princeton University, Princeton, NJ, USA, [3]Albuquerque Seismological Laboratory, U.S. Geological Survey, Albuquerque, NM, USA

Key Points:

- Global microseism wavefields contain extensive spatially averaged and period-dependent information on ocean wave state
- Globally averaged primary and secondary microseism amplitudes have intensified at 0.17 and 0.11%/yr, respectively, since the 1980s
- Microseism amplitudes have intensified in all period bands between 4 and 20 s and have increased most rapidly at the longest ocean wave periods

Supporting Information:

Supporting Information may be found in the online version of this article.

Correspondence to:

R. C. Aster,
Rick.Aster@colostate.edu

Citation:

Aster, R. C., Lee, T. A., Simons, F. J., Ringler, A. T., & Anthony, R. E. (2026). Global primary and secondary microseism multi-decade geographic variation, secular intensification, and period lengthening. *Journal of Geophysical Research: Solid Earth*, *131*, e2025JB032422. https://doi.org/10.1029/2025JB032422

Received 9 JUL 2025
Accepted 26 FEB 2026

Author Contributions:

Conceptualization: Richard C. Aster, Adam T. Ringler
Formal analysis: Richard C. Aster, Thomas A. Lee, Frederik J. Simons, Adam T. Ringler

Abstract Earth's long period background seismic wavefield is dominated by two distinct processes that couple ocean wave energy to a global microseism wavefield. We assess global microseism intensity in the secondary (4–10 s) and primary (14–20 s) bands, and across eight 2 s-wide period bands between 4 and 20 s. Robustly estimated primary and secondary secular amplitude trends are estimated at 73 globally distributed seismic station sites with continuous recording spanning at least 20 years, from as early as the late 1980s through October 2025. These trends are positive at 3σ significance for 61 (84%) and 46 (63%) stations with global average rates for vertical-component acceleration of 0.17 ± 0.04 and 0.11 ± 0.05%/yr, for the primary and secondary bands, respectively, with corresponding rates of energy increase of 0.27 ± 0.08 and 0.15 ± 0.09%/yr. Secular intensification is also observed within all 2 s period bands between 4 and 20 s. Amplitude histories for the longest primary microseism periods (18–20 s) correlate to near-antipodal distances, reflecting long-range teleconnections attributed to large-fetch storm systems, long-range swell and Rayleigh wave propagation, and geographically correlated El Niño Southern Oscillation and other geographically extensive atmospheric influences on storms and waves. The lower average rates of intensification for the secondary microseism suggest that crossing wave systems in remote regions are either under-observed or are intensifying more slowly than the primary microseism, possibly due to increasing swell unidirectionality. Secular intensification is greatest at the longest primary microseism periods. This is consistent with a broadening of the global ocean wave spectrum by approximately 0.01%/yr which may reflect an increasing occurrence of large storm systems.

Plain Language Summary Earth's global seismic background between periods of 4–20 s is dominated by signals created by ocean waves. The primary microseism between 14 and 20 s is generated by direct wave forces on the ocean floor at depths of less than about 350 m. The stronger secondary microseism between 4 and 10 s period arises from crossing wave systems that generate seismic waves at half the ocean wave period. We evaluate period-dependent microseism intensity from the late 1980s through October 2025 at 73 globally distributed seismic stations. 61 (84%) and 46 (63%) of these sites show significant primary and secondary microseism intensification, respectively. Global average rates of 0.17 ± 0.04 and 0.11 ± 0.05%/yr in amplitude and 0.27 ± 0.08 and 0.15 ± 0.09%/yr in energy at 99% significance. Greater rates of intensification for the primary microseism suggest that long-period unidirectional ocean swell is intensifying more rapidly than crossing wave systems. Global average rates of primary microseism intensification are highest at the longest seismic periods, consistent with 0.01%/yr shift in ocean waves to longer periods.

1. Introduction

Earth's global microseism wavefield (Gutenberg, 1947; Omori, 1901) arises from ocean gravity wave seafloor forces. By the mid-20th century it was established that the most energetic part of the microseism spectrum, between approximately 4–20 s, arises from a superposition of two distinct, primary and secondary, source processes whose seismic spectra differently reflect ocean gravity wave spectra. In addition to containing information on global ocean wave state, the microseism wavefield finds extensive use in ambient noise tomography (e.g., Nakata et al., 2019; Shapiro & Campillo, 2004), provides a quasi-coherent large-scale signal for seismic station calibration and quality assessment (e.g., Gal et al., 2019; Lee et al., 2023; Ringler et al., 2014), and establishes the long-period background noise floor for seismic detection and analysis of earthquakes and other seismic events (e.g., Niklasson et al., 2025; Peterson, 1993; Ringler et al., 2022).

Funding acquisition: Richard C. Aster
Investigation: Richard C. Aster, Thomas A. Lee, Adam T. Ringler
Methodology: Richard C. Aster, Thomas A. Lee
Project administration: Richard C. Aster
Software: Richard C. Aster, Adam T. Ringler, Robert E. Anthony
Supervision: Richard C. Aster
Validation: Richard C. Aster
Visualization: Richard C. Aster, Thomas A. Lee
Writing – original draft: Richard C. Aster
Writing – review & editing: Thomas A. Lee, Frederik J. Simons, Adam T. Ringler, Robert E. Anthony

The microseism period range is longer than that of typical anthropogenic noise sources (e.g., Lecocq et al., 2020; Peterson, 1993; Ringler et al., 2022), and thus readily facilitates unobstructed proxy observations of ocean wave state in space, time, and period (e.g., Aster et al., 2008; Aster et al., 2010; Aster et al., 2023; Bromirski, 2023; Bromirski et al., 1999; Grevemeyer et al., 2000; Stutzmann et al., 2009; Tian & Ritzwoller, 2015). Microseism metrics, interpreted in association with oceanographic data, have also been applied to the tracking and wave metric assessment of individual storm systems (e.g., Bromirski, 2001; Ebeling & Stein, 2011) and in regional characterizations of wave state (e.g., Arya et al., 2025; Borzi et al., 2022, 2025; Bromirski, 2023; Gerstoft & Tanimoto, 2007; Minio et al., 2023; Shabtian et al., 2023). Archives of uniform broadband digital seismic records currently approach four decades, and analog data holdings exceed a century (Albeck-Ripka, 2023; Lee et al., 2020; Ringler et al., 2019).

1.1. Primary and Secondary Microseism Source Processes

The primary microseism (PM) manifests as a power spectral density (PSD) shoulder or mode between approximately 14–20 s. It reflects the dynamic pressure field spectrum of ocean gravity waves and associated normal and shear tractions expressed across seafloor bathymetry, and produces seismic excitation at causative ocean wave periods (Ardhuin, 2018; Ardhuin et al., 2019; Gualtieri et al., 2019; Nishida, 2017; Nishida et al., 2008).

For shallow gravity water waves of wavelength λ, the linear-theory dispersion relationship is (e.g., Lighthill, 1996)

$$\omega^2 = gk \tanh(kz) \tag{1}$$

where $k = 2\pi/\lambda$ is the wavenumber, $\omega = 2\pi f$ is the angular frequency, z is water depth, and g is the acceleration of gravity. The corresponding wave-generated dynamic-pressure power spectral density $S_p(f)$ at seafloor depth z_0 is related to the sea surface wave power spectral density $S_w(f)$ as (Dean & Dalrymple, 1991)

$$S_p(f) = \frac{S_w(f)}{\cosh^2(kz_0)} \tag{2}$$

which produces a 95% amplitude falloff for $kz_0 \approx 3.7$ ($z_0/\lambda \approx 0.59$), or for depths of approximately 179 and 366 m for 14 and 20 s ocean waves, respectively. PM energy in this period range is thus nearly exclusively generated within tens of kilometers of island and continental coasts (Figure S1 in Supporting Information S1), which constitutes approximately 11% of the global seafloor (e.g., Dierssen & Theberge, 2014).

The SM spectrum, between approximately 4–10 s, is typically around 40 dB greater in acceleration units than the PM (e.g., Peterson, 1993). It is excited by generalized crossing seas that create half-period high horizontal phase velocity pressure fluctuations on the ocean floor (e.g., Ardhuin et al., 2015; Hasselmann, 1963; Longuet-Higgins, 1950). Due to the necessary condition of crossing seas and period-dependent water column resonance sensitivity to ocean depth, SM source regions (Igel et al., 2021, 2023; Kedar, 2011; Kedar et al., 2008) are generally geographically distinct from PM source regions (Stutzmann et al., 2009) and occur in both shelf and pelagic regions. SM Rayleigh waves generated in the deep ocean, in addition to being remote from most long-term (land-based) seismic stations, encounter strong scattering near continental margins, so observed SM intensity at specific stations is broadly biased toward regional sources, particularly for near-coastal stations (Bromirski et al., 2013; Le Pape et al., 2021; Tanimoto & Anderson, 2023).

Generalized seismogenic ocean wave processes (Ardhuin et al., 2015; Traer & Gerstoft, 2014) also excite additional, much lower amplitude, components within the microseism wavefield. These include body waves (Gerstoft et al., 2008; Landes et al., 2010; Li et al., 2020; Zhang et al., 2010), the 30–300 s Earth hum (Kedar & Webb, 2005; Traer et al., 2012; Traer & Gerstoft, 2014), and microseism contributions to Earth's normal modes (e.g., Nawa et al., 1998; Webb, 2008).

2. Data and Analysis

We examine global period-dependent microseism intensity spanning the PM and SM bands using 1 sample/s seismograms beginning at the inception of standardized global digital broadband seismographic networks in the late 1980s and extending through 30 October 2025. We utilized EarthScope Data Services to retrieve vertical-

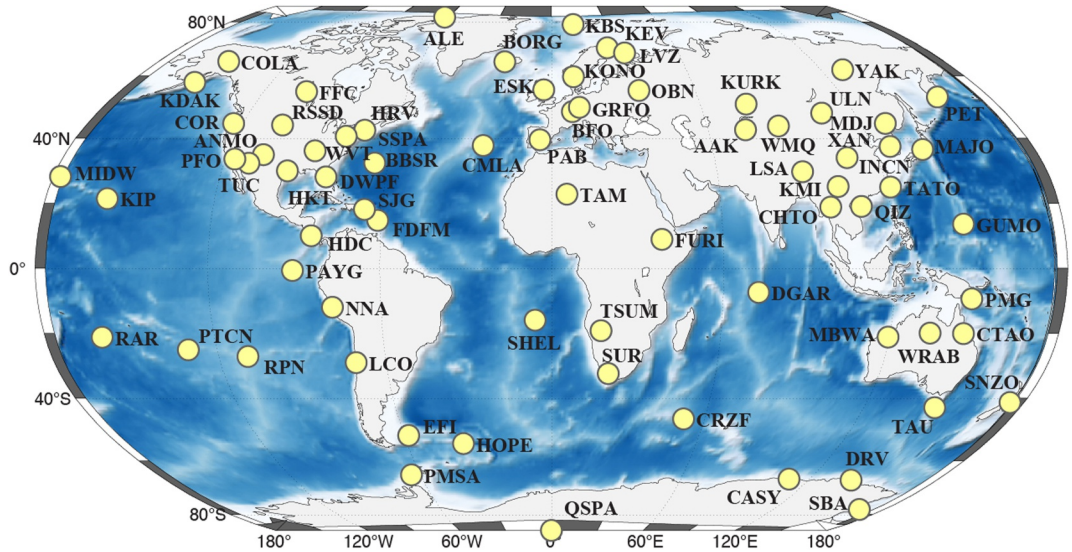

Figure 1. Seismic station sites in this study (Table S1 in Supporting Information S1) from the Global Seismographic (FDSN IU/II; 10.7914/SN/IU and 10.7914/SN/II; Ringler et al., 2022; Davis, 2024), New China Digital (IC; 10.7914/SN/IC; Anderson et al., 2015), and GEOSCOPE (G; 10.18715/GEOSCOPE.G; Leroy et al., 2023) networks. Stations were selected for >20 years of data and >75% data completeness.

component data from stations in the Global Seismographic (FDSN IU/II; 10.7914/SN/IU and 10.7914/SN/II; Ringler et al., 2022; Davis, 2024), New China Digital (IC; 10.7914/SN/IC; Anderson et al., 2015) and GEOSCOPE (G; 10.18715/GEOSCOPE.G; Leroy et al., 2023) networks with >20 years of data and >75% data completeness. These criteria identified 73 stations, with 49 in the Northern Hemisphere and 24 in the Southern Hemisphere (Figure 1, and Figure S2; Table S1 in Supporting Information S1) and incorporates approximately 3.2 years of additional data and 21 additional sites compared to the global PM study of Aster et al. (2023). The longest data records analyzed (HRV and ESK; Harvard Massachusetts and Eskdalemuir, Scotland) span approximately 37.8 years (approximately 1.2×10^9 data points at 1 sample/s).

We calculate microseism absolute amplitude and energy envelopes within 2 s-wide period bands by integrating acceleration power spectral density estimates (PSDs). PSDs are estimated in hourly 50% overlapping moving windows from 1 sample/s continuous seismic data and are corrected for instrument response to units of $(m/s^2)^2/Hz$. PSD integrals are calculated using the trapezoidal rule for period bands $[P_1,\ P_2]$, and the square root of these integrals produces semi-hourly sampled time series $A(t,\ P_1,\ P_2)$ in acceleration units, where t is the PSD window center time. Vertical-component seismic data in the microseism period range are dominated by Rayleigh waves, and are thus insensitive to Love waves and to Rayleigh wave propagation direction.

For the 73 stations of Figure 1 we integrate PSDs in 2 s bands centered at 19, 17, 15, 13, 11, 9, 7, and 5 s. Square root PSD integrals may be mapped to velocity or displacement within these narrow bands by dividing once or twice, respectively, by $\omega = 2\pi/\bar{P}$ where $\bar{P}$ is the band center period. It has been verified that the observations and conclusions in this study are fundamentally unchanged for seismic velocity or displacement time series data, and we largely focus here on results from vertical acceleration time series.

We remove data for time intervals that are potentially influenced by earthquake Rayleigh waves using origin times from the U.S. Geological Survey (USGS) Advanced National Seismic System Comprehensive Earthquake Catalog (ComCat; USGS, 2017) for event magnitudes greater than or equal to 5.75, using a slightly modified version of the algorithm used in Aster et al. (2023) (see Text S1 and Figure S3 in Supporting Information S1).

Time series obtained from integrating hourly 50% overlapping PSD intervals for the earthquake-culled data are resampled from semi-hourly to 1-day intervals using 48-point non-overlapping medians. One-day sampled time

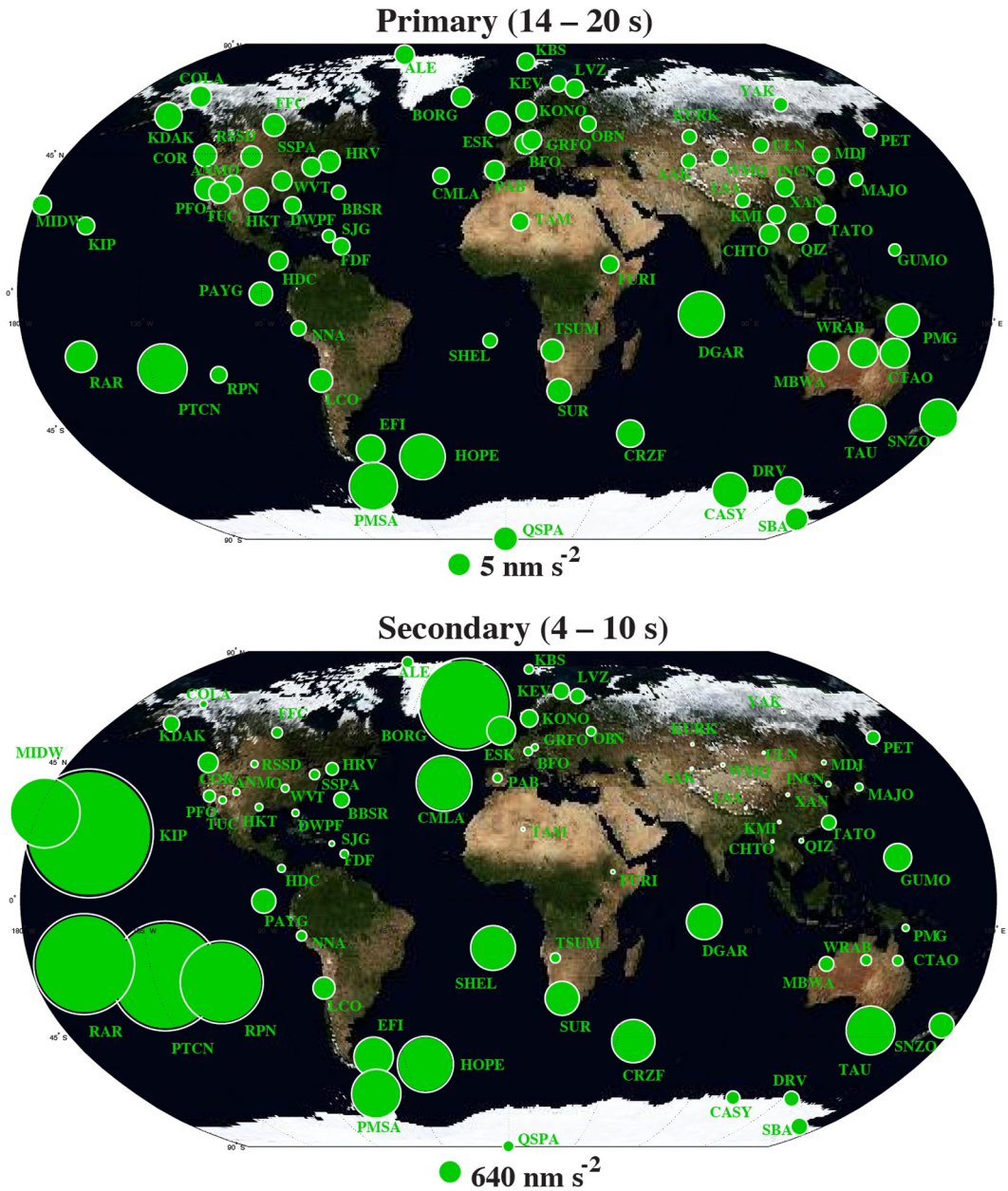

Figure 2. Median vertical-component acceleration amplitudes (Tables S2 and S3 in Supporting Information S1) scaled to circle diameter for the stations of Figure 1. Top: Primary band (PM; 14–20 s); Bottom: Secondary band (SM; 4–10 s). SM band medians are typically 2–3 orders of magnitude larger than PM counterparts (Peterson, 1993) and have greater mean to median separation reflecting higher time series variance (Figure S4 in Supporting Information S1).

series are subsequently smoothed to emphasize multi-month-scale variations using longer-duration (e.g., $T_0/6 \approx 60.9$ days or $3T_0$) moving median windows, where $T_0 = 365.2422$ days is the tropical year.

2.1. Median Amplitudes

Figure 2 shows geographical global median PM and SM variations, including high amplitudes that reflect the particularly high ocean wave energy of the Southern Ocean (e.g., Chen, 2024; Reguero et al., 2019; Young & Ribal, 2019). Compared to the PM, SM median amplitudes display much greater general geographical variability and localization, much smaller values within continental interiors compared to coastal regions, and very large values at ocean islands (e.g., Hawai'i (KIP), Iceland (BORG), and Pitcairn Island (PTCN)).

PM and SM amplitudes in Antarctica are strongly influenced by seasonal sea ice, which attenuates or blocks ocean waves at near-shore PM and SM source zones during the mid-winter extratropical storm peak (e.g., Anthony et al., 2017; Aster et al., 2008; Cannata et al., 2019; Grob et al., 2011; Pratt et al., 2017). This effect shifts the annual microseism amplitude peak for continental Antarctic stations (QSPA, CASY, DRV, and SBA) earlier in the year by one to 3 months and, by restricting near-continent waves during the austral winter, results in lower median microseism amplitude values than would otherwise be observed. Seasonal microseism signal influences of sea ice are generally much less in the Arctic than for the Antarctic at the periods examined in this study but are significant at shorter periods (e.g., Baker & Abbott, 2022; Chen et al., 2025; John & West, 2025; Tsai & McNamara, 2011).

2.2. Primary and Secondary Band Secular Trends

We estimate ℓ_1 misfit norm-minimizing secular linear trends for each site as functions of period in time series units per year (R_A) and as proportional trends in percent per year (P_A) obtained by normalizing R with respect to median for the entire time series (Figure 2), that is, for vertical-component acceleration,

$$P_A = R_A/\mathrm{med}(A(t)) \times 100\%. \tag{3}$$

Where useful, such as in comparisons with other sea state studies, we also calculate secular linear trends for seismic energy (e.g., P_E), using identically processed velocity-squared vertical amplitude time series. PM and SM band results are obtained by PSD integration for the period intervals 14–20 s and 4–10 s, respectively. Period range- and station-specific stationary annual variability functions, $H(t)$, for PM and SM bands, and for individual 2 s bands, are estimated using zero-mean four-term least-squares Fourier series fits for each time series with fundamental period T_0,

$$H(t) = \sum_{n=1}^{4} c_n \sin(2\pi n t/T_0 - \theta_n). \tag{4}$$

Annual harmonic functions calculated for each station and microseism band and are subtracted prior to final secular trend estimations. Examples of PM and SM data processing, annual harmonic functions, and trend fitting for four stations are shown in Figures S5 and S6 of Supporting Information S1.

Global PM and SM proportional acceleration trends for $T_0/6 \approx 60.9$-day median-smoothed times series ranked by PM trend, are shown in Figure S7 of Supporting Information S1, and in map view in Figure 3. Notably, SM trends have greater geographic and general variation relative to PM trends, and PM trends display higher average values. PM and SM trends are significantly correlated (Pearson coefficient $R = 0.63$ with an associated p-test value of 3×10^{-9}; Figure 4), and the bivariate ℓ_1 SM versus PM trend regression line has a slope of 1.04 ± 0.05 and a y (SM) intercept of -0.05 ± 0.01%/yr indicative of systematically lower SM trends, with appreciable scatter.

Figure 5 shows station-median-proportional PM and SM time series medians for all stations with $3T_0$ moving-window median temporal smoothing to emphasize multiyear variations, with the global average of ℓ_1 misfit norm-minimizing station linear trends from 60.9-day smoothed time series (0.17 ± 0.04 and 0.11 ± 0.05%/yr, respectively; 3σ confidence) plotted in red. For the more station-complete (Figure S2 in Supporting Information S1) data interval beginning on 1 January 2000, PM and SM global average trends (0.19 ± 0.05 and 0.11 ± 0.07%/yr, respectively) are only marginally different from those calculated using the complete data set.

Average global energy trends for the PM and SM velocity squared energy proxy are 0.27 ± 0.08 and 0.15 ± 0.09%/yr. Prominent global multiyear excursions in Figure 5 reflect the widespread intensification of waves in the Western and Eastern Pacific during positive and negative excursions, respectively, of the El Niño-Southern Oscillation (ENSO) (Barnard et al., 2015; Odériz et al., 2021), as discussed in Aster et al. (2023) for the PM. Figure 5 shows that these excursions also occur for the SM but are generally much less pronounced.

2.3. Period-Dependent Secular Trends

We also examine more general time series and secular trend behavior, using all 2 s-wide PSD integral bands (with center periods of 19, 17, 15, 13, 11, 9, 7, and 5 s) across the microseism spectrum, noting that there will likely be

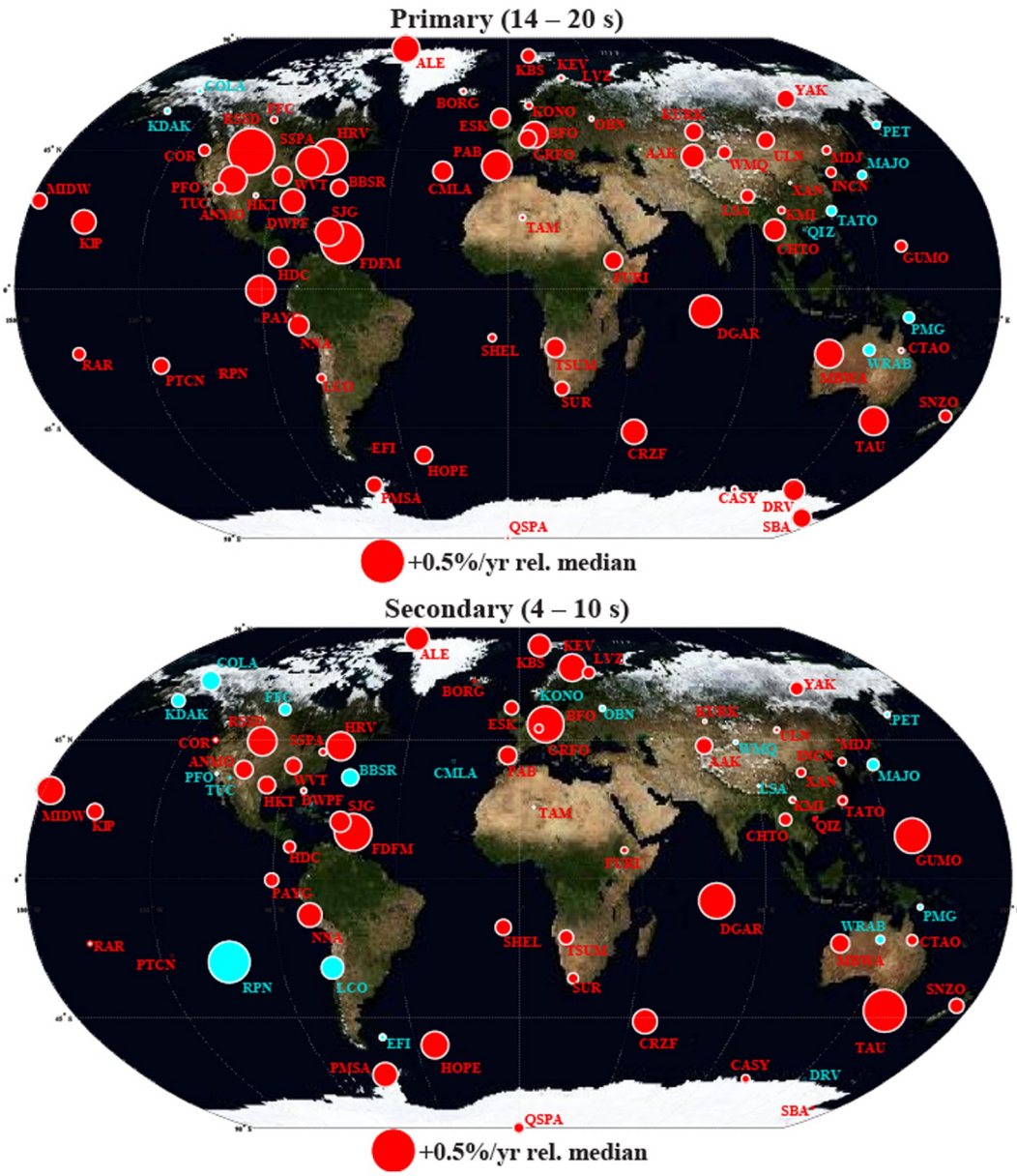

Figure 3. Map views of Primary (PM) and Secondary (SM) band vertical-component acceleration amplitude median-proportional-trends P_A (Figure S7; Tables S2 and S3 in Supporting Information S1).

variably superimposed PM and SM source contributions in the crossover periods around 10–12 s (Figure 6). Figure S8 in Supporting Information S1 shows an example of comparative secular trends at station HRV for all 2 s period bands and for the 14–20 s PM and 4–10 s SM bands, and including the time-dependent time series coefficients of variation

$$c_{\text{var}} = \sigma(A)/\bar{A} \tag{5}$$

that characterizes the mean-normalized variation of each time series. In line with global average observations, SM band period-dependent trends at example station HRV are both lower and show much greater period dependence than for the PM bands. SM band time series also show higher values of c_{var} indicating greater and/or more frequent transient mean-relative excursions, and consistent with the nonlinear relationship between SM source strength and wave amplitude (e.g., Ardhuin et al., 2011).

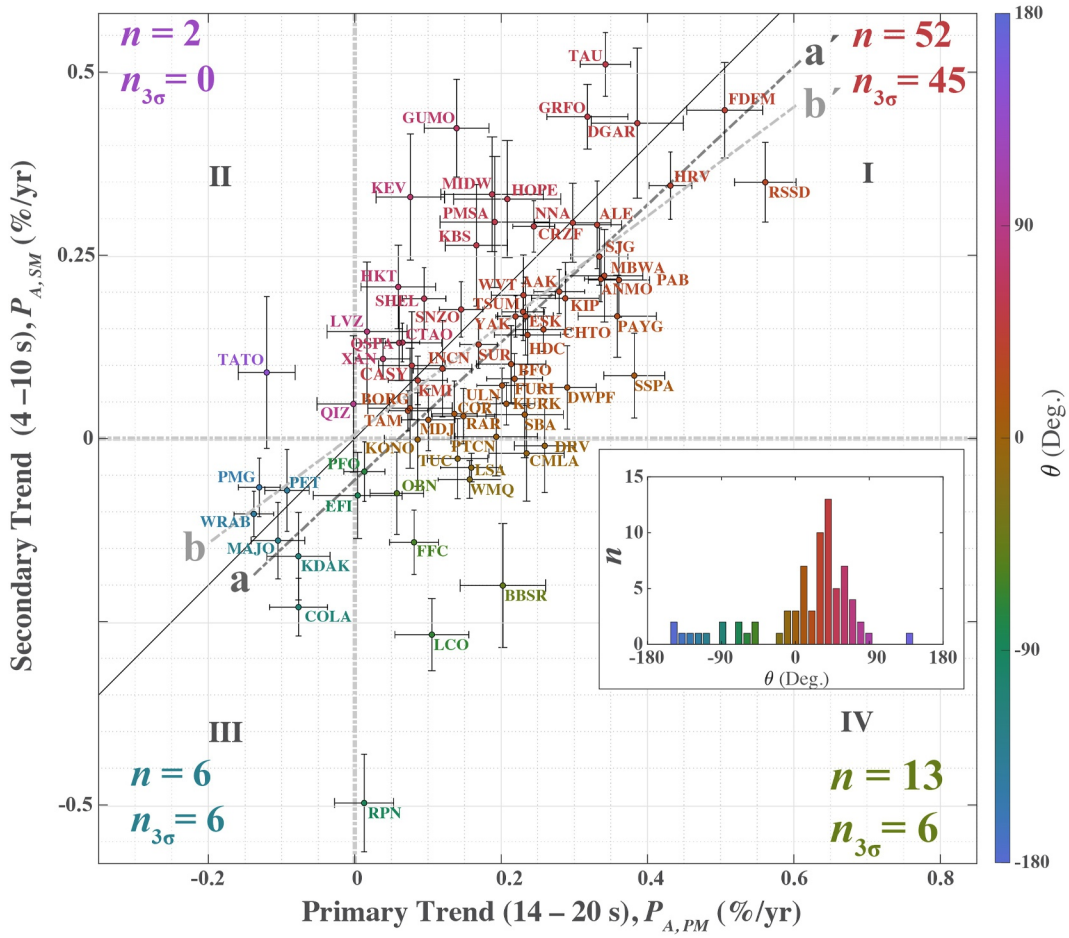

Figure 4. Secondary (SM) versus primary (PM) vertical-component acceleration proportional trends (P_A; Figures S3 and S7, and Tables S2 and S3 in Supporting Information S1) with 3σ confidence intervals. Coupled trend populations by quadrant are given in the legend, categorized by the angle with respect to the origin $\theta = \arctan(P_{A,SM}, P_{A,PM})$ (color bar at right). n and $n_{3\sigma}$ indicate number of points, and number of points with 3σ confidence, respectively, in each quadrant (I–IV). The solid line is a $\theta = 45°, 135°$ equality reference through the origin. The darker dashed line is a bivariate ℓ_1 norm misfit minimizing regression line (a–a′) that has a slope of 0.93 ± 0.05 and SM intercept of -0.05 ± 0.01%/yr. The bivariate fit (b–b′) to the 3σ-confidence populations using only $(P_{A,PM}, P_{A,SM})$ points with joint consistent positive and negative trends has a slope of 0.75 ± 0.03 and an SM intercept of $8 \times 10^{-4} \pm 8 \times 10^{-3}$%/yr. Pearson correlation is 0.63. Inset figure shows the distribution of θ for all stations.

Figure 7 shows 2 s period band global median P_A time series and trends in the format of the PM and SM time series in Figure 5, showing 1σ median confidence corridor widths that generally increase at shorter periods. ENSO-associated multiyear amplitude oscillations (see Aster et al., 2023) are most apparent in the PM bands (14–20 s) and in the 8–10 s SM band, and are poorly resolved or unresolved for period bands between 4 and 8 s.

Correlations between the detrended 3-year smoothed time series of Figure 7 are shown in Figure 8, as well as corresponding correlations (annual stationary harmonic variations and linear trends removed) for time series with smoothing lengths of 2 years, 1 year, and 60.9 days. Common features in the subplots of Figure 8 are high-correlations within the PM (14–20 s) bands, and between PM bands and corresponding half-period SM bands. In contrast, time series for SM periods are much less globally correlated, and 4–6 s band timeseries are largely decorrelated from all other bands.

Figure 9 shows proportional trend estimates P_A and coefficients of variation for all stations collected in each period band, showing kernel densities, with data points from example station HRV (Figure S8 in Supporting Information S1) highlighted for reference. The coefficient of variation c_{var} across the station population is lowest

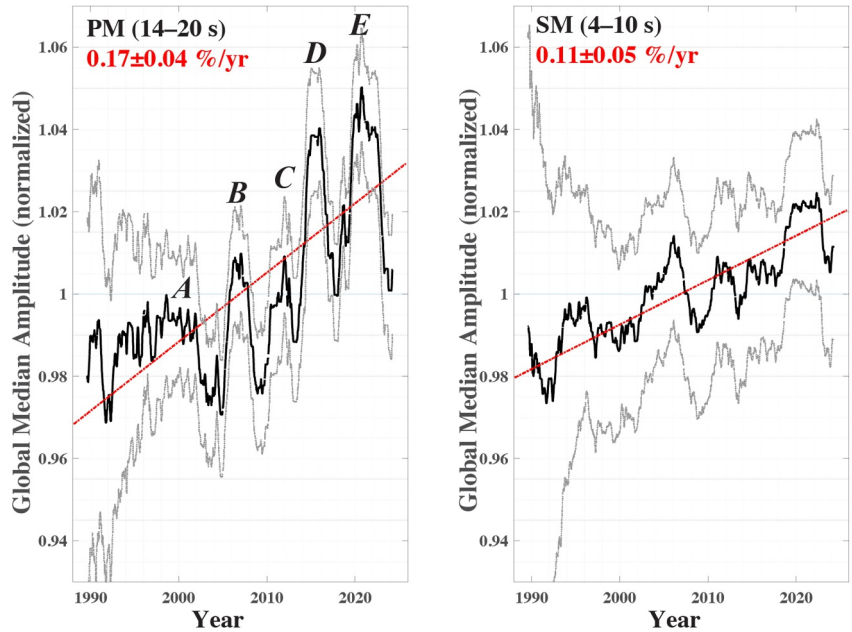

Figure 5. Primary (PM) and secondary (SM) band vertical-component acceleration median-proportional amplitudes (Equation 3) with 3-year median smoothing to emphasize multiyear variations. The global median of all time series with individual annual stationary harmonic variations (Equation 4) removed (e.g., Figures S5 and S6 in Supporting Information S1) is shown in black with a one-standard-deviation corridor. Average linear trends calculated from 60.9-day smoothed data are shown in red. Series are normalized to a mid-interval value of one. Reductions in uncertainty corridors with time reflect increasing numbers of seismic stations (Figure S2 in Supporting Information S1). The multiyear maxima in the PM (A–E), and to a lesser extent in the SM, are correlated with ENSO and SOI (El Niño-Southern Oscillation and Southern Oscillation Index) variations, particularly for sites in the Southwest Pacific and Southeast Pacific/Southwest Atlantic regions, respectively (see Figure 7 of Aster et al., 2023).

within the PM band and highest within the SM band, peaking at 8–10 s. A positive median rate of secular amplitude increase is observed in every 2 s band at 3σ significance with the exception of 6–8 s, which is positive at 2σ significance.

2.4. Times Series Correlations With Interstation Distance

Interstation correlations (2,628 station pairs) of period-dependent station amplitudes with $T_0/6 \approx 60.9$-day moving-median smoothing, stationary annual harmonic functions (Equation 4) subtracted (e.g., Figure S9 in Supporting Information S1), and linear trends removed, are displayed with respect to interstation separation as point density plots of Figure 10. This figure thus displays period-dependent correlation on regional to global scales of non-seasonal microseism variations at approximately bimonthly and longer time scales. Geographic correlation scale length generally increases with period. The shortest significant correlation distances of $\lesssim 20°$ occur for the 4–6 s SM band, beyond which the mean correlation population becomes indistinguishable from zero. Conversely, characteristic station-pair correlation distance approaches near-antipodal distances at 18–20 s. Greater correlation distances compared to adjacent bands is also apparent for periods near 8–10 s, consistent with the highlighted enhanced off-diagonal elements of the inter-band correlation matrix in Figure 8. These observations further indicate globally extensive temporal correlations between PM- and SM-causative wave systems in 2:1 period-band pairs, and show that this condition is particularly strong between the 16–20 s PM and 8–10 s SM bands.

To further examine the geography of period-dependent microseism amplitude correlation, we map interstation time-history PM to SM correlations C to corresponding station-station great-circle paths for $C > 0.2$ (Figure 11) and within each 2 s period band (Figure 12). Also shown in these figures (station color groups) are best-fit period-dependent correlation clusters ($N = 10$) obtained using the Ward distance metric. High correlations are associated with interstation great-circle paths that transit cratonic regions of North America, Eurasia, and Australia. Ocean-transiting interstation paths that likely reflect long-range swell influences are also observed, and become

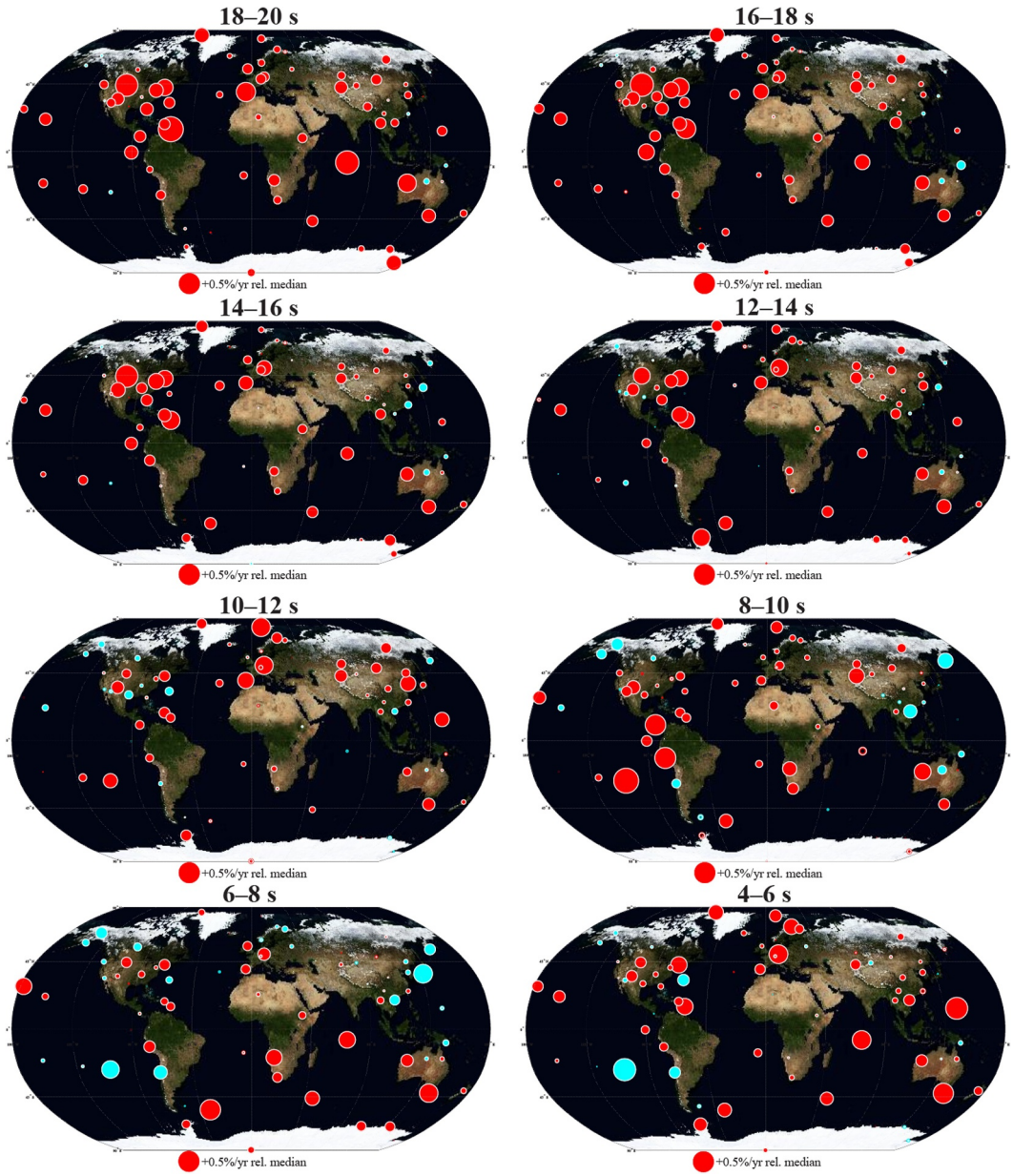

Figure 6. Map views of global vertical-component acceleration median-proportional secular trends P_A (%/yr) in each indicated 2-s period band (Tables S4–S12 in Supporting Information S1).

increasingly pronounced at longer periods. Some $C > 0.2$ correlation great circles span distances exceeding 10,000 km, exemplified by interstation paths connecting the South Pacific and Western North America, crossing the Indian Ocean, and between Antarctica and other continents in both the Southern and Northern hemispheres. The longest-range correlations are most apparent in the 16–20 s PM bands and in its corresponding half-period 8–10 s SM band. Since secondary microseism-band Rayleigh waves ocean paths may be poorly observed or unobserved due to ocean-continent scattering (Bromirski et al., 2013; Le Pape et al., 2021; Tanimoto & Anderson, 2023), long-distance continental correlation paths seen in the 8–10 s SM band may indicate geographically extensive ocean swell systems reflecting off local coastlines (e.g., Class II SM source mechanism; Ardhuin et al., 2011). In contrast, PM Rayleigh wave energy propagates more effectively across greater distances (Hearn, 2024; Ma et al., 2015; Park et al., 2005) including across ocean basins (Anthony et al., 2017; Cessaro, 1994; Lin et al., 2006).

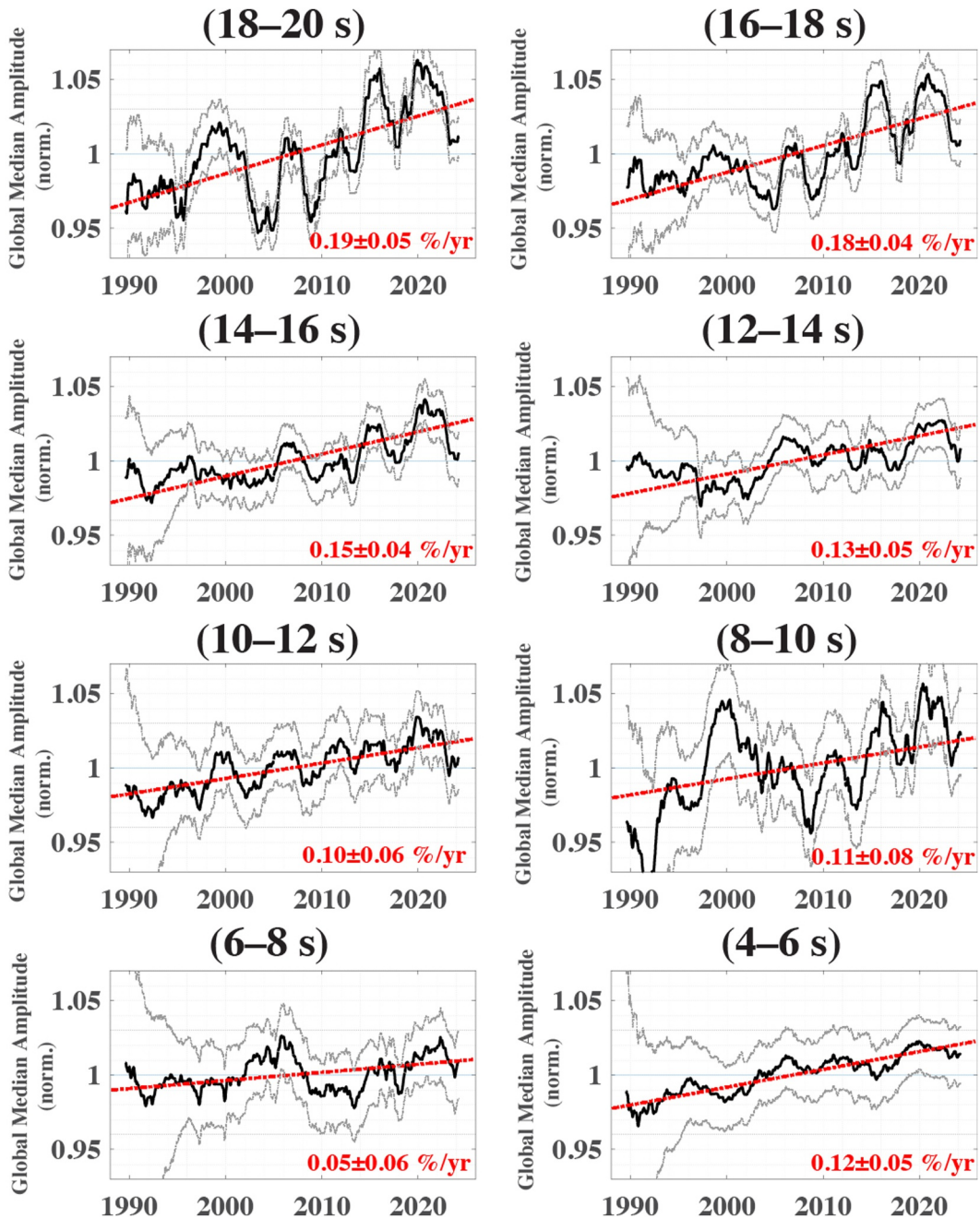

Figure 7. Global vertical-component acceleration in 2 s wide period bands corresponding to Figure 6 displayed identically to the PM and SM band time series in Figure 5.

3. Discussion

3.1. Secondary Source Non-Linearity and Enhanced Coefficients of Variation

A consistent observation is that SM time series show systematically higher coefficients of variation relative to PM time series (Figure 9, and Figures S4 and S10 in Supporting Information S1). We examine this relationship and its further implications for understanding geographically widespread divergent microseism metrics between PM and SM.

PM sources reflect spatio-temporally integrated tractions arising from the ocean bottom pressure field acting on bathymetry (Equation 2; Figure S1 in Supporting Information S1). Under linearized assumptions for an otherwise

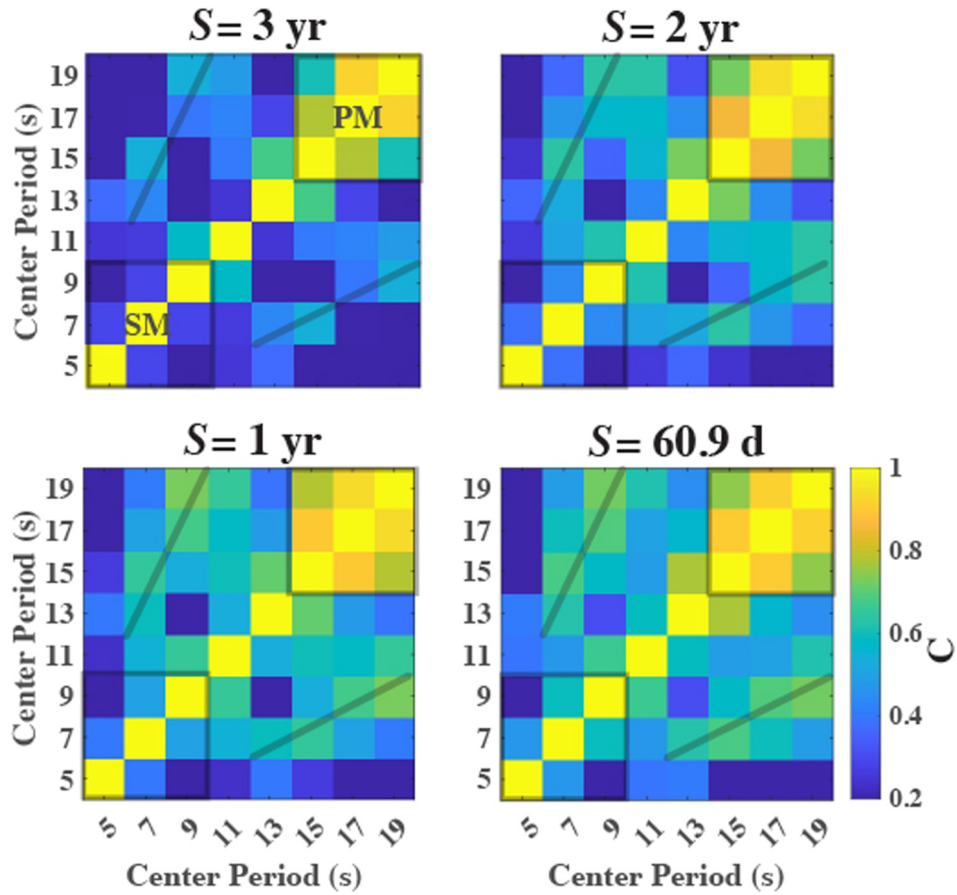

Figure 8. Correlations, C, between linearly detrended global median time series in 2 s wide period bands with four different temporal smoothing window lengths S between 3 years and 60.9 days, where the $S = 3$-year median figure at upper left shows correlations between the eight median time series of Figure 7. All individual station time series contributing to the global median time series had annual harmonic functions subtracted and were demeaned prior to correlation. PM and SM labels denote primary and secondary microseism band ranges of 14–20 s and 4–10 s, respectively. Larger inter-band PM correlations indicate much higher spatial correlation in PM wavefield intensity relative to the SM. Off-diagonal bands (grey lines) highlight swaths of increased global correlation at period ratios of 2:1, indicating correlated SM to PM amplitudes consistent with common causative ocean wave states.

stationary ocean wave field, the time-smoothed seismic displacement time series u_{PM} will be proportional to time-smoothed wave height B_{PM} at the same period T (Ardhuin et al., 2011; Hasselmann, 1963)

$$u_{PM}(T) \propto B_{PM}(T). \tag{6}$$

SM sources are inherently nonlinear. For two crossing wave state components with amplitudes B_{SM} and B'_{SM} at period T, SM source strength at period $T/2$ will be proportional to the amplitude product (e.g., Ardhuin et al., 2011; Longuet-Higgins, 1950; Traer & Gerstoft, 2014). SM displacement amplitude under otherwise stationary conditions in this case will scale as

$$u_{SM}(T/2) \propto B_{SM}(T)B'_{SM}(T). \tag{7}$$

more generally, SM amplitude scaling represents the spatiotemporal integration of directionally distributed crossing seas arising from classes of SM source wave conditions defined in Ardhuin et al. (2011): (a) broad swell-band directional spectra arising from a single storm system (Class I) (Traer & Gerstoft, 2014); (b) coast-reflected swell (Class II); (c) intrastorm crossing swell (Class IIIa); or (d) interstorm crossing swell (Class IIIb).

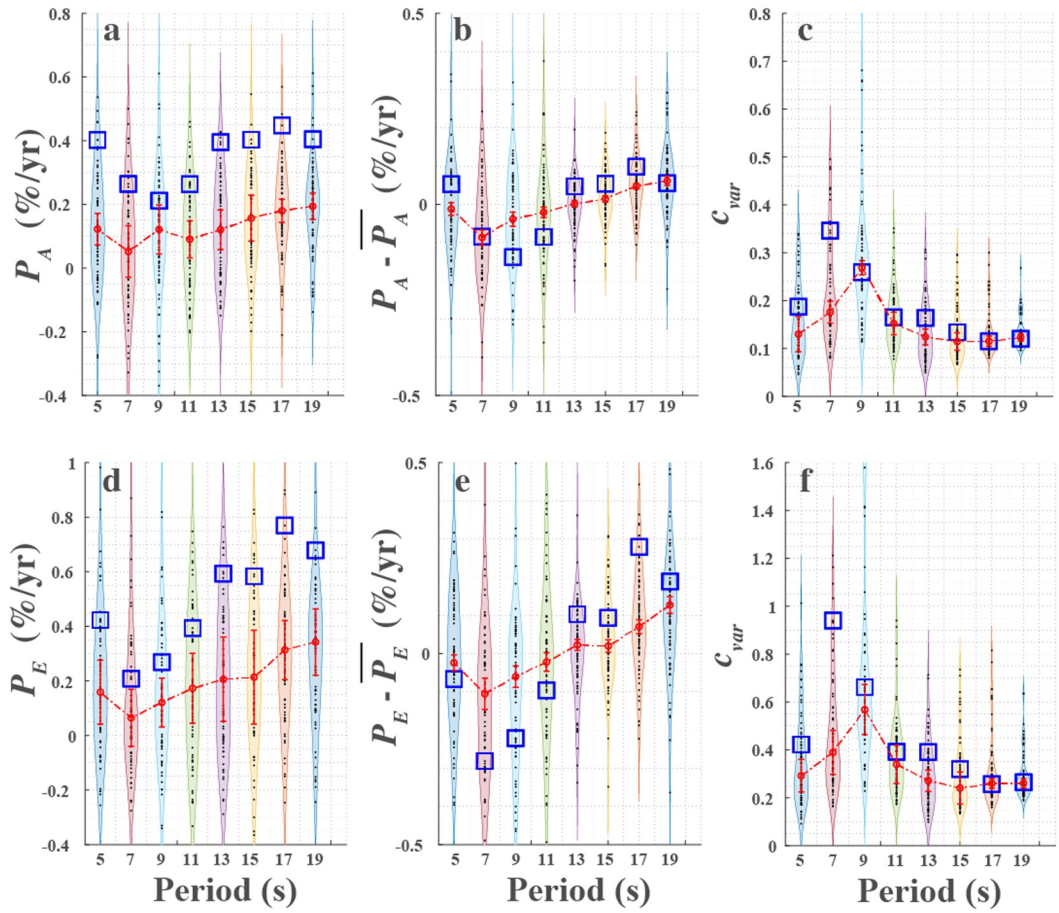

Figure 9. Global proportional secular vertical-component acceleration amplitude trends P_A (Equation 3) and coefficients of variation as a function of period for all stations (Figure 1) (black dots) with moving-median temporal smoothing of $T_0/6 \approx 60.9$ days and seasonal harmonic functions (Equation 4) subtracted. Colored swaths show kernel density estimates within each period band, with representative results for station HRV (Figure S8 in Supporting Information S1) shown as blue boxes. Median values and associated 3σ confidence intervals estimated using bootstrap statistics for each period band are shown in red. (a) Proportional trends. (b) Proportional trends from (a) with the average trend across all bands for each station, $\overline{P_A}$, subtracted. (c) Corresponding coefficients of variation (Equation 5). (d–f) Corresponding energy (velocity-squared) trends, P_E, and coefficients of variation.

In comparing long-term records of PM and SM amplitudes we consider the statistical relationship at each station as a site-specific mixture of two end-member cases. In the first case, SM half-period energy is produced by wave systems that incorporate contemporaneous PM-generating swell, and u_{PM} and u_{SM} will thus be temporally correlated. Correlation could intermittently occur for each of the SM wave system classes, but will be assured for Class II wave systems since they result from interfering incoming and coastal reflected swell that traverses PM source zones. For Class I and III wave systems, SM half-period energy may be generated independently of contemporaneous PM-generating swell and u_{PM} and u_{SM} will thus be less correlated, or uncorrelated. The degree to which the different SM source wave classes contribute to SM intensity will be reflected in the statistical SM to PM microseism intensity history at a given site. Additional factors affecting this relative history will include the suitability of regional bathymetry for strong SM excitation and regional specific ocean-continent-station geography and geology. At some stations, such as lower latitude island sites that are seismically sensitive to swell from both hemispheres, the statistical SM to PM amplitude relationship may show seasonal dependence due to annual variations in wave directionality. However, to the degree that long-term wave state evolves solely due to wave amplitude, geographic and geological influences can be usefully assumed to constitute a station-specific "site effect" when averaged over many years.

We parameterize long-term microseism SM versus PM variations at individual stations using a simple power law model

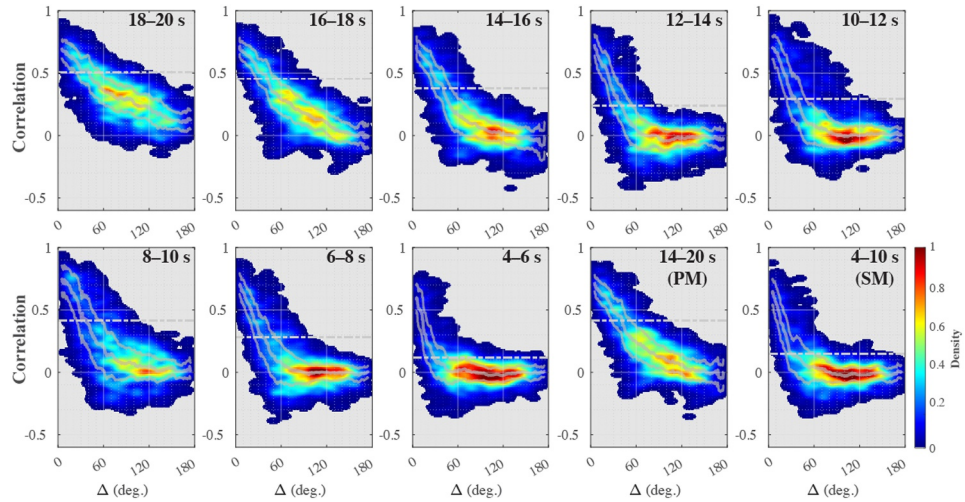

Figure 10. Interstation vertical-component acceleration history (median temporal smoothing of $T_0/6 \approx 60.9$ days, detrended, and with annual harmonic functions subtracted) correlation density for (2,628) station pairs with respect to interstation angular distance Δ. Subplots show each 2 s period band, and the PM (14–20 s) and SM (4–10 s) bands. Correlation population median and median, plus and minus one mean absolute deviation, calculated in moving 10° angular windows are shown in gray. Horizontal gray lines indicate 84% correlation distribution percentiles (mean plus one standard deviation). Note statistically slower correlation falloff with interstation distance with increasing period, and evidence for near-antipodal correlation for some stations at the longest PM periods. Kernel density bin widths are 2° in angular distance and 0.01 in correlation.

$$u_{SM}(T/2) = \alpha(T)\ (u_{PM}(T))^p\ . \tag{8}$$

For sites where long-term PM and SM amplitudes are poorly correlated we expect $p \approx 0$, and α to characterize the amplitude ratio $u_{SM}(T/2)/u_{PM}(T)$. For highly correlated PM and SM amplitudes, such as those arising from persistent coastal reflections (Class II) from a quasi-linear coastline, where a largely oppositional wave-directional distribution results in strong SM generation (e.g., Hasselmann, 1963), we expect $p \approx 2$, and α characterizes the strength of the coastal reflection and relative efficiencies of relevant PM and SM sources. Broadly favorable conditions for PM-correlated SM energy are present, potentially due to contributions from all SM excitation wave classes, may correspond to $p \gtrsim 2$.

PM and SM coefficients of variation can also be modeled within the framework of Equation 8 by noting that the coefficient of variation ratio between two time series X and αX^p is

$$R_{c_{\text{var}}}(p) = \frac{c_{\text{var}}(X^p)}{c_{\text{var}}(X)} = \frac{\sigma(X^p)/\mathbb{E}[X^p]}{\sigma(X)/\mathbb{E}[X]} \tag{9}$$

where $\mathbb{E}$ denotes the expected value operator. Figures S11 and S12 in Supporting Information S1 display the approximate log-normality of the observed PM and SM time series amplitude distributions (i.e., normality of log amplitude), and we consider this simplifying case going forward. For a log-normal distributed time series $X = e^Z$ where Z is $N(\mu, \sigma_L^2)$. In this case

$$\mathbb{E}[X^p] = e^{p\mu + \frac{1}{2}p^2\sigma_L^2} \tag{10}$$

$$\text{Var}(X^p) = e^{2p\mu + p^2\sigma_L^2}\left(e^{p^2\sigma_L^2} - 1\right) \tag{11}$$

$$c_{\text{var}}(X^p) = \frac{\sqrt{\text{Var}(X^p)}}{\mathbb{E}[X^p]} = \sqrt{e^{p^2\sigma_L^2} - 1} \tag{12}$$

and the coefficient of variation ratio is between αX^P and X is

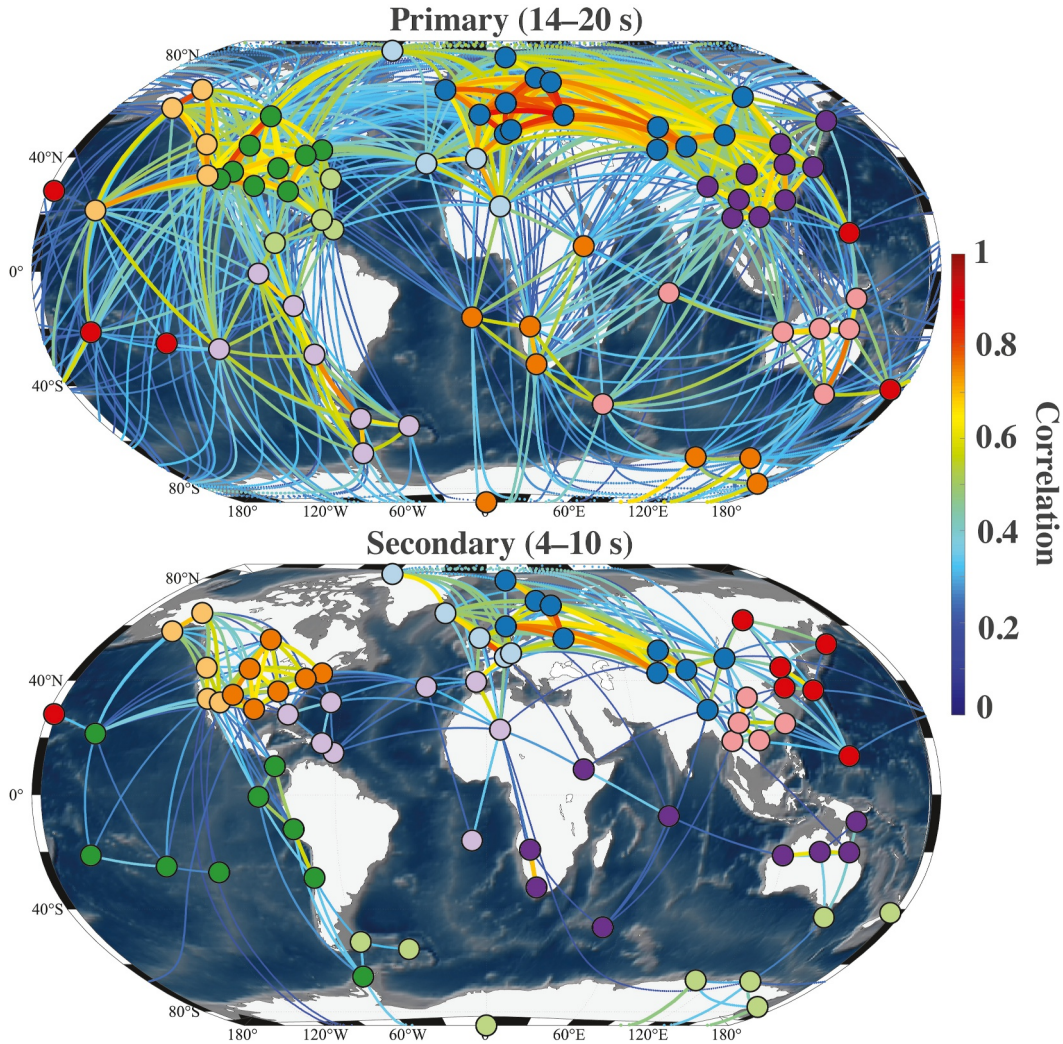

Figure 11. Great circle correlation paths and Ward metric similarity clusters (station colors) for the primary (PM; top) and secondary (SM; bottom) bands. Great circle paths for $C > 0.2$ are distinguished by color as indicated in the color bar (Figure 10, and Figure S9 in Supporting Information S1).

$$R_{c_{\text{var}}}(p) = \frac{\sqrt{e^{p^2\sigma_L^2} - 1}}{\sqrt{e^{\sigma_L^2} - 1}} \approx |p| \quad \left(\sigma_L^2 < 1\right). \tag{13}$$

For $p > 1$ and small values of σ_L^2, Equation 13 predicts larger coefficients of variation for SM time series relative to double-period PM counterparts, as is broadly observed, and empirical PM and SM values of σ_L^2 are 0.064 ± 0.05 and 0.25 ± 0.21, respectively (1σ), so the limiting case in Equation 13 is relevant (Figure S13 in Supporting Information S1).

We examine the multi-decade statistical applicability of Equations 8 and 13 for all stations by comparing PM data in the 16–20 s band with its exact (half-period) 8–10 s SM counterpart given that these bands display evidence of globally widespread PM to SM correlation (Figures 5, 7, and 8). We estimate α and p via robust (ℓ_1 misfit norm-minimization) fitting of Equation 8 in log-log space

$$\log u_{SM}(T/2) = \log \alpha + p \log u_{PM}(T) \tag{14}$$

using 60.9-day median smoothed SM and PM displacement amplitude time series.

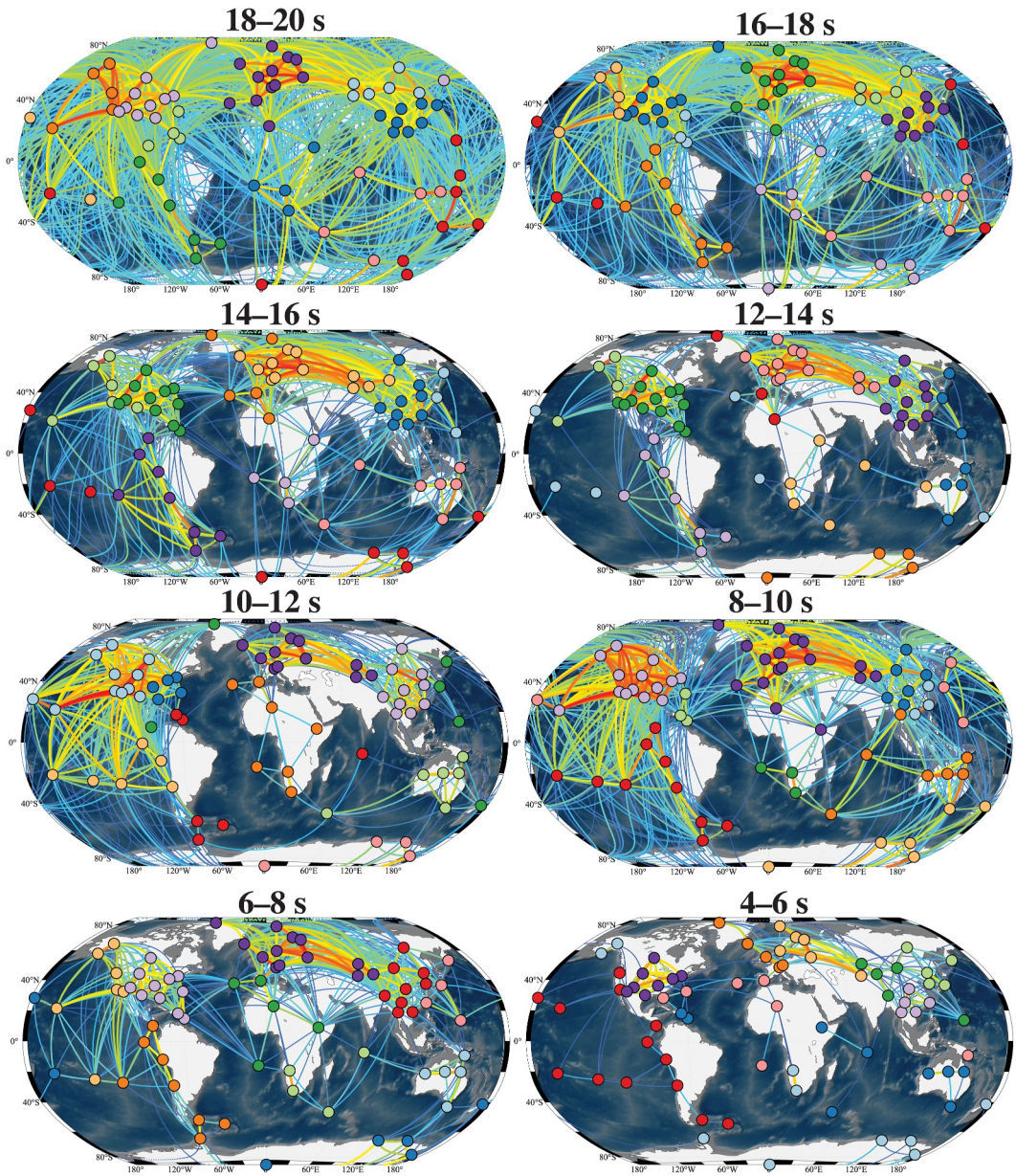

Figure 12. Period-dependent (2-s bands) great-circle correlation paths for $C > 0.2$, and station clusters, displayed as in Figure 11 (Figure 10, and Figure S9 in Supporting Information S1).

Parameter estimations, coefficients of variation, data variances, and data correlations are shown in histograms in Figure S13 of Supporting Information S1. Estimates of the exponent p range from 0.06 (QIZ, Qiongzhong, China) to 3.2 (MIDW, Midway Island, USA) and average 1.68 ± 0.73. Figure 13 show poorly and highly correlated example station fits to Equation 14, and SM versus PM plots in this format for all stations showing corresponding values of p are shown in Figure S14 of Supporting Information S1. SM to PM fits to the power law relationship degrade considerably when broader and non-2:1 period ratio bands are compared, reflecting apparently strong period-dependence of SM source processes and intensities (Figure S15 in Supporting Information S1).

Figure 14 shows $R_{c_{\text{var}}}$ (Equation 13) versus p (Equation 8) (y and x axes), and correlations ρ of the log-transformed PM-SM data (e.g., Figure 13) in symbol color. Stations with high ρ values (dark red symbols) are relatively well fit by Equation 8 and trend toward the limiting case of $R_{c_{\text{var}}} = p$, consistent with approximately log-normal signal

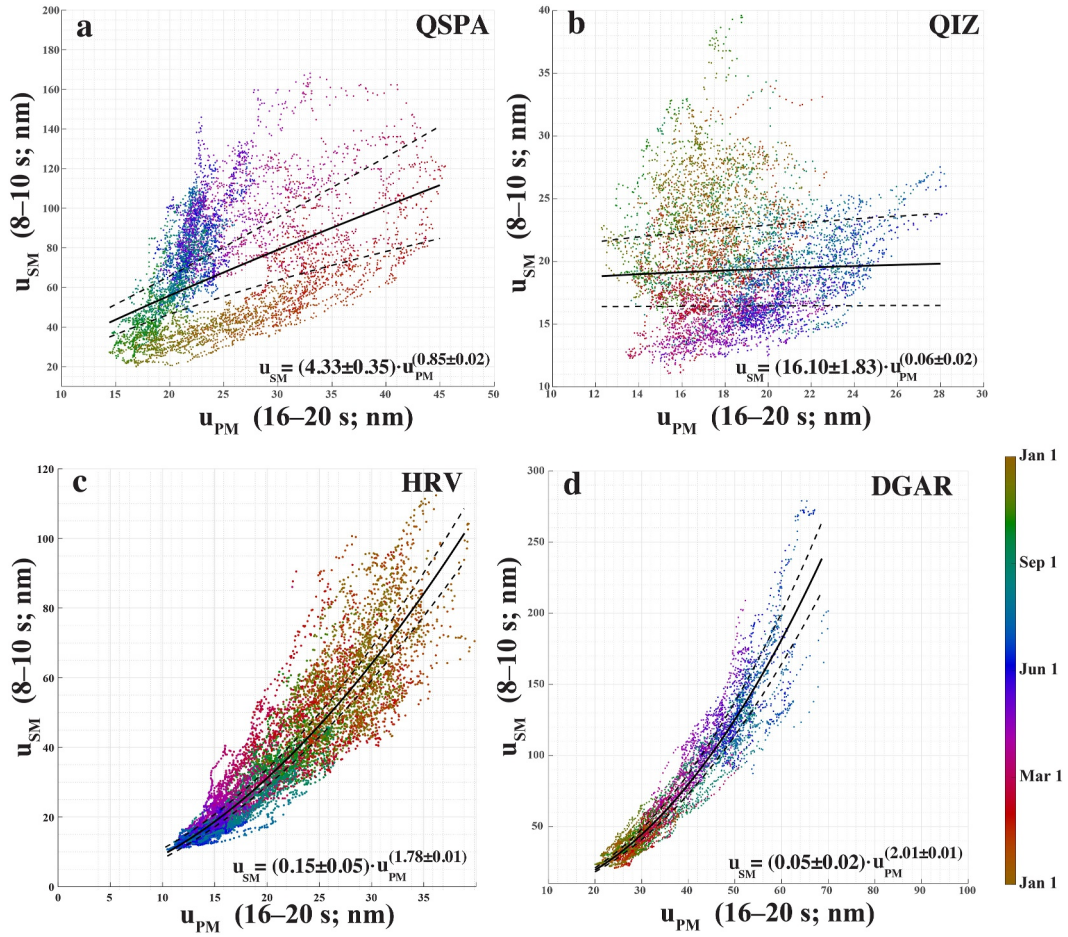

Figure 13. Example sites with low (a, b) and high (c, d) SM (8–10 s) to PM (16–20 s) vertical-component displacement amplitude ($T_0/6 \approx 60.9$-day median smoothing) correlations. Daily data point colors indicate annual phase (circular color bar). Model fits (Equation 8) are shown as black curves with 3σ variation (dashed envelopes) in exponent p. (a) QSPA (South Pole). $p = 0.85 \pm 0.02$, time series duration is 22.6 years, and the Pearson correlation of the log-transformed data is $\rho = 0.47$. (b) QIZ (Qiongzhong, China). $p = 0.06 \pm 0.02$, time series duration is 24.7 years, and the Pearson correlation of the log-transformed data is $\rho = 0.04$. QSPA and QIZ show strong seasonal variations in (u_{SM}, u_{PM}) that produce low multiyear power law signal correlation ρ. (c) HRV (Harvard, Massachusetts). $p = 1.78 \pm 0.01$, time series duration is 37.8 years, and the Pearson correlation of the log-transformed data is $\rho = 0.93$. (d) DGAR (Diego Garcia). $p = 2.01 \pm 0.01$, time series duration is 21.8 years, and the Pearson correlation of the log-transformed data is $\rho = 0.96$. HRV and DGAR maintain u_{SM} versus u_{PM} power law proportionality throughout the calendar year.

characterization (Equation 13). Large-scale and systematic geographic variations in these parameters are also apparent, with sites in North America and Western Eurasia, and some ocean islands (e.g., Figures 13c and 13d) displaying $p \gtrsim 2$ and thus indicating strong wave state correlation between PM and SM sources. This is consistent with strong SM excitation due continental and island coast scattering and other crossing wave conditions in relative continent-dominated Northern Hemisphere compared to the ocean-dominated Southern Hemisphere.

Values of $p > 2$, corresponding to particularly high SM to PM intensity ratios (Figure 2) occur for some island sites (TATO, MIDW, KDAK, TAU, RPN, KDAK), for some sites near coastlines with large expanses of adjoining contiguous ocean (NNA, CTAO, PET, PMG), and are not strongly latitude dependent. High SM intensity at these sites may reflect extensive ocean wave scattering into regional SM source zones by the Class II mechanism, superimposed with highly active class I and III SM source zones due to open ocean wave-wave interactions that may reduce overall SM to PM correlation ρ. Low-correlation stations outside of the Antarctic also exhibit significant seasonality in SM to PM behaviors that likely reflect seasonal variations in wave direction due to bihemispheric wave sensitivity (Figure S14 in Supporting Information S1).

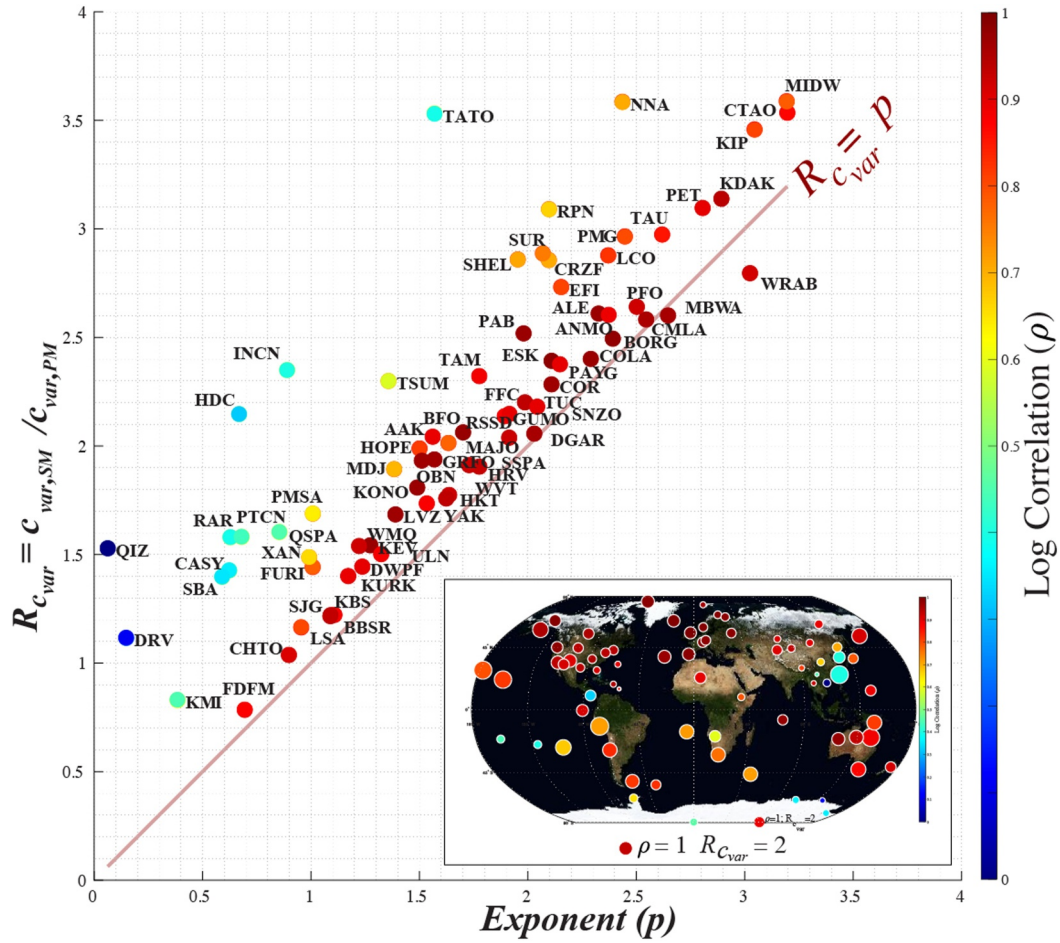

Figure 14. Secondary (SM) to primary (PM) vertical-component displacement coefficient of variation ratio $R_{c_{\mathrm{var}}}$ (Equation 13) versus exponent p (Equation 8). Symbol colors indicate PM-SM log amplitude correlation ρ (color bar). Inset: Map displaying $R_{c_{\mathrm{var}}}$ (symbol diameter) and ρ (same color scale as in the main figure). Red line shows the theoretical limiting case for power law data behavior and small values (<1) of log data variance predicted by Equation 13 for log-normal distributed data (Figures S11 and S12 in Supporting Information S1).

A notable cluster of low ρ stations is also apparent in East Asia, which we examine further below in Section 3.3.3. Continental Antarctic stations (QSPA, CASY, DRV, and SBA) have notably low ρ values caused by strong seasonal decorrelation between PM and SM time series due to ocean wave attenuation and screening by near-coastal sea ice (Figures 13a and 13b; Pratt et al., 2017; Anthony et al., 2017). This produces a counterclockwise annual orbital in SM versus PM time amplitudes for these four since the growth of sea ice from the coast preferentially reduces PM amplitude relative to SM amplitude early in the calendar year (March–May) by attenuating swell and PM source basal swell tractions in shallower near-coastal waters (Figures 13c and 13d).

The period band-dependent coefficients of variation shown in Figure 9, and Figure S10 of Supporting Information S1, are estimated from time series that have had annual harmonic functions (Equation 4) H subtracted, since the subtraction of these zero-trend variance-increasing data projections improves the accuracy of secular trend estimates (e.g., Figures S5 and S6 in Supporting Information S1; Aster et al., 2023). For each time series X the subtracted seasonal function H is a zero-mean Fourier series fit, so the residual $E = X - H$ is orthogonal to H, $\sigma_X^2 = \sigma_H^2 + \sigma_E^2$, and the coefficient of variation becomes

$$c_{\mathrm{var}}(X - H) = c_{\mathrm{var}}(X)\sqrt{1 - \phi} \tag{15}$$

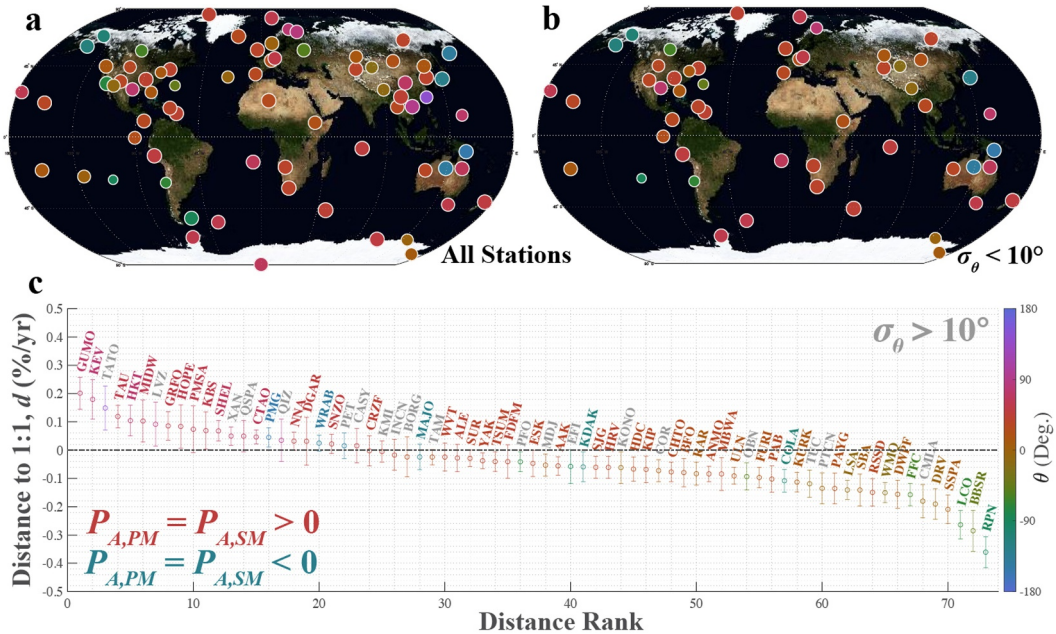

Figure 15. Top: Maps corresponding to Figure 4, with station colors indicating relative rates and signs of SM versus PM median-normalized secular change. (a) All stations; (b) Stations (53) with well-resolved quadrant angles θ ($\sigma_\theta < 10°$). Station symbol size is proportional to $1 - |(d)|$, where d is the vertical bivariate point distance from $P_{A,SM} = P_{A,PM}$ in Figure 4, shown in (c). Relatively poorly resolved stations ($\sigma_\theta > 10°$) are indicated in (c) in gray. Stations with $P_{A,SM} > P_{A,PM}$ have positive values of d, and stations with $P_{A,SM} < P_{A,PM}$ have negative values of d. Positive and negative trend equality conditions correspond to red and cyan, as indicated at lower left.

where $\phi = \sigma_H^2/\sigma_X^2$ is the variance-based fit of H to X. The subtraction of stationary seasonal functions thus results in the de-seasonalized (ds) SM to PM coefficient of variation ratio

$$R_{c_{\mathrm{var,ds}}} = R_{c_{\mathrm{var}}} \cdot \sqrt{\frac{1-\phi_{SM}}{1-\phi_{PM}}} = R_{c_{\mathrm{var}}} \cdot q\ . \tag{16}$$

The subtraction of (frequently large; Figures S5 and S6 in Supporting Information S1) seasonal amplitude variations from u_{PM} and u_{SM} reduces correlation but has only a limited effect on their coefficient of variation ratios. This occurs because the SM and PM seasonal Fourier station variance-based fits (ϕ_{PM} and ϕ_{PM}) are generally positively correlated (Pearson correlation 0.66) and the modifying term q in Equation 16 is thus close to 1 at most stations, with empirical values of $q = 1.10 \pm 0.25$ (Figures S16 and S17 in Supporting Information S1).

3.2. Global Average Primary and Secondary Trends

Robustly estimated secular amplitude trends from the 73 widely distributed seismic stations are positive at 3σ significance for 61 (84%) and 46 (63%) stations with global average rates of 0.17 ± 0.04 and 0.11 ± 0.05%/yr, for the PM and SM respectively, with corresponding rates of energy increase of $P_E = 0.27 \pm 0.08$ and 0.15 ± 0.09%/yr (3σ confidence). Average acceleration and energy trend ratios between the SM and PM are thus 0.65 and 0.55, respectively. The average primary rates determined in this study are consistent with those calculated in Aster et al. (2023) who found $P_E = 0.27 \pm 0.03$%/yr for a subset (52) of these stations with an approximately 3.2-year shorter record. As in Aster et al. (2023), we examine metric consistency to ensure that the gradual build-out of the seismic networks and increasing number of global stations meeting our completeness and duration criteria (Figure S2 in Supporting Information S1) do not significantly bias results. We assessed this by comparing all-data results and results obtained using only data collected after 31 December 1999. Pairs of estimates from these two data intervals overlap at 3σ confidence, for example, global average acceleration trends P_A for the SM are 0.11 ± 0.05 and 0.10 ± 0.07%/yr, and for the PM are 0.17 ± 0.04 and 0.19 ± 0.05%/yr (3σ confidence), for all data and for post-1999 data, respectively.

Average estimated energy intensification rates in this study for both the PM and SM are significantly lower than those estimated for global average wave energy increase in other studies, notably Reguero et al. (2019) who estimated a global average rate of 0.4%/yr and a rate of 0.58%/yr for the Southern Ocean across multiple decades. The discrepancy may reflect seismic insensitivity in the SM band to wave power increase in the Southern Ocean due to sparse station coverage in the Southern Hemisphere, and lower levels in PM bands may reflect the inherent near-coastal bias of the PM source mechanism.

Comparative metrics for the Southern and Northern Hemispheres shows somewhat higher rates of energy intensification for the Southern Hemisphere in amplitude and energy at low significance in the primary band ($P_{E,SH} = 0.30 \pm 0.09$%/yr and $P_{E,NH} = 0.26 \pm 0.07$%/yr for the PM) and more significant higher rates of change in the SM band ($P_{E,SH} = 0.21 \pm 0.10$%/yr and $P_{E,NH} = 0.12 \pm 0.08$%/yr; 3σ confidence). Higher rates of secular SM energy change in the Southern Hemisphere are consistent with independent estimates of multi-decade wave state intensification for the ocean basins. For example, Reguero et al. (2019) estimated secular wave energy change in a joint altimetry and modeling analysis corroborated by buoy measurements for the global ocean and noted that the highest rate of inferred intensification occurred in the Southern Ocean, consistent with earlier estimates derived from compilations of multi-mission satellite altimetry data for 1985–2008 (Young et al., 2011). These comparative hemispherical rates (see also Figure S10 in Supporting Information S1 also suggest that we do not have strong southern hemisphere insensitivity to wave state in these data.

3.3. Comparative Primary and Secondary Secular Trends

The nonlinear SM vs. PM amplitude modeling and coefficient of variation analysis in Section 3.1 is consistent with observed larger SM trend confidence intervals (Figure S7 in Supporting Information S1, Figures 4 and 5) and with systematically higher SM coefficients of variation. Secular intensification is significantly positive for all period bands spanning the PM and SM at 3σ significance except for the 6–8 s band, which is positive at 2σ significance (Figure 7), and the globally observed individual station SM versus PM rates are significantly correlated, with significant scatter (Figure 4); Pearson correlation of 0.63, with an associated p-test value of 3×10^{-9}). General period-dependent trend structure is also apparent in Figures 3 and 6 and worthy of further study, but we will mostly restrict this discussion to the differing rates of secular change estimated for the PM (14–20 s) and SM (4–10 s) bands.

To further examine relative rates of PM and SM change in geographic context, we plot key features of Figure 4 in map view in Figure 15. Some stations that plot close to the origin in Figure 4 have low estimated trends and higher uncertainties in angular classifications. 19 stations have quadrant angle uncertainties $\sigma_\theta > 10°$ (Figure 4), and we show maps with and without these relatively poorly constrained stations in Figure 15. We discuss prominent individual and multistation features of joint PM and SM trend variation below.

3.3.1. Joint Primary and Secondary Secular Trends

Forty five stations, distributed across both Northern and Southern Hemispheres and in all ocean regions, have jointly positive PM and SM trends at 3σ significance (Figures 3 and 4), and are shown in Figure 15 in colors that are close to red on the figure color wheel. This population represents 62% of all stations and 79% of all stations where quadrant assessments in Figure 4 can be made at 3σ significance. Robust regressions for both the full station population and the population restricted to sites with jointly significant nonzero PM and SM rates (labeled (a) and (b) in Figure 4) corroborate a lower average global rate of SM secular change. General fits to global populations with 2 s band ranges (Figure 5) also show greater average trend intensification as period increases across the microseism spectrum (Figures 6 and 9) with the exception of the shortest (4–6 s) band, which is poorly correlated with all other bands (Figure 8). General global intensification in both bands is thus pervasive, but interesting exceptions exist, as discussed below.

3.3.2. Negative Secular Trends

Six stations in the Northern and Western Pacific region (COLA, KDAK, WRAB, MAJO, PMG, PET) have jointly negative PM and SM trends at 3σ significance, and are shown in Figure 15 in colors that are close to cyan on the figure color wheel. This group is not reflected in correlation-based clustering based on de-seasonalized and detrended long-term station histories (Figures 11 and 12; Aster et al., 2023) since station history correlations are much more strongly influenced by multiyear ENSO and other year-to-year transient variations (Figures 5 and 7)

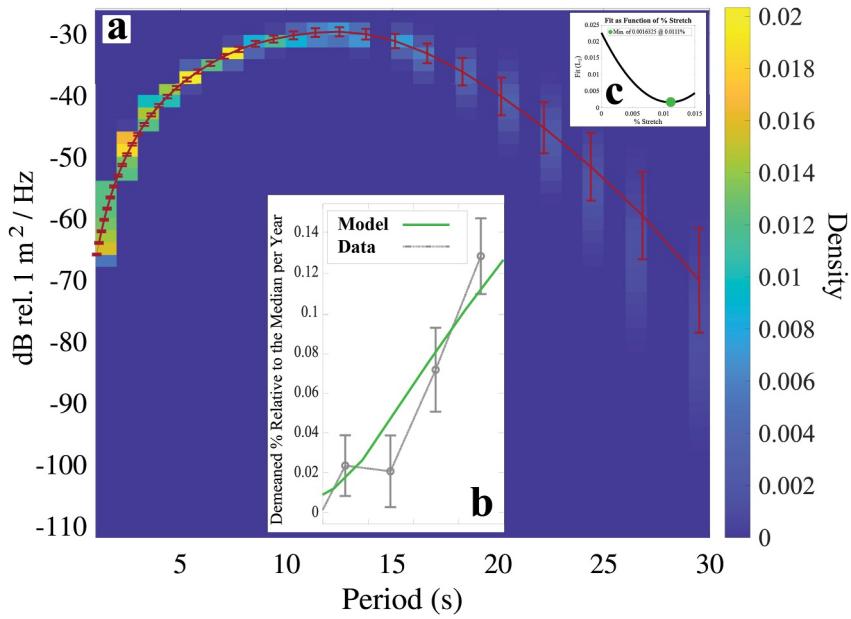

Figure 16. (a) Power spectral reference density probability density of global average wave height from 1991 to 2024 archives of global WAVEWATCH III runs; WAVEWATCH Center (2019). The red curve displays the average PSD with 1σ variability given by vertical bars. (b) Theoretical fit (green) of period-dependent energy trends corresponding to spectral stretching of about 0.01%/yr (Figure S18 in Supporting Information S1). Gray data points with 3σ error bars indicate observed globally averaged seismic energy trends between 12 and 20 s from Figure 9e. (c) ℓ_2-norm residual between theoretical and observed rates of power change as a function of spectral stretching factor with optimal solution highlighted (Equation 17).

than by secular trends (e.g., Figures S5 and S6 in Supporting Information S1). Joint PM and SM secular microseism amplitude decline at these sites is most prominent in the PM (14–20 s) band and longer period (6–10 s) SM bands (Figure 6) where general signal variation is well correlated in Figure 14. Trends for the Alaskan and Northwestern Pacific sites in this group are consistent with decadal-scale Northern and Western Pacific satellite altimetry estimates of declining significant wave height (Young & Ribal, 2019) and with wave hindcast reanalysis for recent decades (Bromirski et al., 2013; Erikson et al., 2022). Some authors have attributed this trend to intensification of the negative phase of the Pacific-North America teleconnection (PNA) since the 1990s (Sasaki, 2014) associated with a tendency for a weaker jet stream and an increased occurrence of blocking high pressure systems in the Northern Pacific that reduce storminess and regional wave generation. The Southwestern Pacific station pair (WRAB, PMG) is distal from the others in this group and their amplitude histories otherwise cluster with stations in the region (Figure 11). Negative trends for these stations likely reflect an independent ocean wave state variation of unknown and local character that does not correlate with prior estimates of secular wave energy assessment such as Erikson et al. (2022), to our knowledge.

Six widely distributed sites (OBN, LSA, WMQ, FFC, LCO, BBSR) have significantly positive PM rates and significantly negative SM rates, and 22 stations in total show PM and SM trend estimates with opposite signs and/or where one or both trend cannot be distinguished from zero at 3σ confidence. Ten of these sites (BORG, KONG, MDJ, KONO, TUC, COR, RAR, PTCN, SBA, DRV, CLMA) have significantly positive PM trends and three (RPN, EFI, PFO) have significantly negative SM secular rates. There are no sites for which the PM trend is significantly negative at 3σ confidence while the SM trend is significantly positive, although TATO is nearly so. There is only one site (QIZ) for which both the SM and PM trends are indistinguishable from zero at 3σ confidence.

3.3.3. Unusual Microseism Features of the South and East China Sea Regions

The population of stations with lower trend rate and higher standard deviation, and thus higher values of σ_θ, includes a group of sites in East Asia (TATO, XAN, MDJ, INCN, KMI, QIZ) that exhibit unusually energetic and seasonally variable local SM source excitation (e.g., Xiao et al., 2018), strong regional interstation history correlations (Figure 11), and low SM to PM amplitude correlations (e.g., Figures 13a and 13b) that are inconsistent

with the power law model (Equation 8; Figure 14). As a result these stations have unusually large $P_{A,SM}$ uncertainties (Figure 4) and diverge from the $R_{c_{\text{var}}} = p$ line in Figure 14. Station QIZ is additionally notable in being the only station in this analysis that lacks 3σ significance for nonzero trend in both the PM and SM bands. The intense and bi-seasonal nature of the SM microseism in this region appears to reflect wave focusing and interference in the South China sea due to cyclonic and other storms that, along with favorable bathymetry and coastline geometry, produces unusually strong SM intensity during typhoon and other regional wave events that is not correspondingly reflected in PM intensity (Arya et al., 2025).

3.3.4. Ocean Islands

Statistically significant outliers in Figures 4 and 15 occur for some remote island sites (e.g., GUMO, RPN, BBSR). However, isolated island stations overall plot on both sides of one-to-one reference line in Figure 4, and such sites also include examples that are close to the central distribution (e.g., DGAR, RAR). The Southeastern Pacific includes two well-resolved sites (RPN, LCO) that exhibit the globally highest negative SM trends (Figure S6c in Supporting Information S1) that may reflect wave reductions since 2010 associated with decreased regional storminess due to westward expansion and intensification of the South Pacific Anticyclone toward Rapa Nui (Easter Island) (Markovitz & Steiger, 2025).

3.4. Global Primary Band Intensification With Period

Global mean and median measures of PM microseism intensity show significantly higher rates of secular change with increasing period (Figures 7 and 9). This effect is comparable in size and period dependence for stations in the Southern and Northern Hemispheres (Figure S10 in Supporting Information S1) suggesting that it represents a widespread feature of microseism and causative wave state change.

To model this observation to first-order, we perturb a unimodal time-averaged mean hindcast model of the global wave spectrum $S_w(T)$ determined by 1991–2024 hindcasts from Figure 16; WAVEWATCH Center (2019), linearly re-mapping its spectral period by a small perturbation $1 + \epsilon$ while keeping total spectral power constant with a spectral power normalization factor. This re-mapping modifies the spectral slope and this change may then be fit to the observed relative intensification slope with period to estimate ϵ. For a positive (period-lengthening) ϵ the perturbation from the reference spectrum will be positive at periods exceeding the reference wave spectrum peak of 11 s, and will be negative at shorter periods (Figure S18 in Supporting Information S1). Because we fit the observed period-to-period variations and not absolute trend values in this exercise, the procedure is not sensitive to the spectral power normalization factor.

Because PM coupling coefficients with respect to ocean wave period (Equations 1 and 2) can be estimated from bathymetry, period-dependent seismic observations can be modeled from ocean wave spectral perturbations (here globally, but also regionally). Although detailed small-scale effects due to bathymetric coupling (Ardhuin et al., 2019) are not well established, time independence and approximate linearity in period-dependent PM source coupling, can be reasonably assumed over decades. Using perturbed spectra, we apply bathymetrically determined (Figure S1 in Supporting Information S1) period-dependent global PM coupling coefficients (Equation 2) for perturbed reference spectra using a 0.5-degree gridded ocean to predict differential changes in the globally averaged PM-dominant microseism spectrum between 12 and 20 s (Figure S4 in Supporting Information S1). Even with the simple assumption of a representative global wave spectrum and the inability to model local-scale PM source regions (e.g., near isolated ocean islands) we can obtain a useful order-of-magnitude measure of the degree of ocean wave spectral stretching consistent with the observed global average secular PM trend inter-period slope.

The falloff of spectral energy at the longest swell periods with increasing period is very rapid (e.g., Ardhuin et al., 2025a), and the reference spectrum of Figure 16 has a power falloff with period T of approximately 40 dB between 15 and 30 s, corresponding to $\approx T^{-13}$ across this interval. Therefore, detectable PM-band progressive inter-period intensification in secular trend may occur, even for small values of ϵ. Conversely, significant observed period-dependent changes in wave intensity with period provide a highly sensitive constraint on ocean wave spectral change at long periods under these modeling assumptions.

Figure 16 demonstrates that introducing a period stretching of a reference spectrum $S_w(T)$ of $\epsilon \approx 0.01\%$/yr, that is,

$$S'_w(T) = cS_w(1.0001 \cdot T) \quad (17)$$

where c is a re-normalization factor to preserve total spectral energy, produces predictions consistent with observed global long-period relative energy trends between 12 and 20 s (Figure 9). This highlights a sensitivity of central tendency microseism observations that is well suited for investigations of large-scale and long-term ocean wave state changes, benefiting from the natural integration of wave forces across extensive geographic regions over multi-decade observational intervalsmultiple decades and the extensive teleconnectivity of ocean and seismic wavefields (Figure 12).

A hypothesis that is consistent with spectral broadening at long swell periods in recent decades is an increasing occurrence of larger storms. Swell at periods greater than about 18 s, where we observe the highest rate of PM intensification, is generated by wind fields exceeding 20 m/s acting across fetch regions that exceed 1,000 km (Meucci et al., 2023; WAM Group, 1988) and can have disproportionate coastal impacts (e.g., Earlie et al., 2015). Some studies have suggested that the number of weaker extratropical cyclones may decrease under global change scenarios, while a small population of stronger storms may conversely intensify (Michaelis et al., 2017; Shaffrey et al., 2013; Shaw & Miyawaki, 2023; Ulbrich et al., 2009). For example, Priestley and Catto (2022) explored seasonal extratropical storm tracks under multiple scenarios and observed the highest increases in wind speed for the largest end-members of the storm population. Cheung and Chu (2023) additionally noted that a consistent process contributing to storm intensification may be an increasing likelihood for tropical cyclones to transform into or intensify extratropical storm systems as they move to higher latitudes (e.g., Bromirski, 2001), an effect which they estimated to be relevant for about 25% of global storms. Although our estimate of ϵ is small, it is consistent with a compounded rate of 0.1%/decade, and this hypothesis may thus be testable using other wave metric measurements.

3.5. Hypotheses for Lower Global Rates of Secondary Microseism Intensification Relative to Primary Microseism Intensification

Globally lower rates of SM intensification compared to the PM may partially reflect under-observation of SM source regions that are undergoing intense crossing sea intensification. This could occur because of poor SM source efficiency in some regions due to unfavorable ocean depth resonance and/or to Rayleigh wave scattering at the continental margin that inhibits land observations of remote ocean SM source regions (Bromirski et al., 2013; Le Pape et al., 2021; Tanimoto & Anderson, 2023), sparse station coverage in the Southern Hemisphere. However, this under-observation hypothesis is inconsistent with similar SM to PM intensification rate differences for well-observed microseism source regions of the Northern Hemisphere, such as the North Atlantic (e.g., Sergeant et al., 2013), and the SM to PM average amplitude secular intensification ratio for the 19 sites closest to the North Atlantic (0.62) does not significantly differ from that of the full global station constellation (0.64). We also note generally similar PM and SM secular trends and trend ratios for the Northern and Southern Hemispheres and conclude that other effects drive these global SM and PM trend differences beyond relative sparse instrumentation of the Southern Hemisphere.

Each seismic site has unique period-dependent microseism sensitivities to the ocean wave state. These differences are controlled by microseism source locations and by their seismic efficiencies, by geography (including bathymetry, which has differing period-dependent influences on PM and SM source processes), and by seismic wave propagation (including Rayleigh wave scattering at continent-ocean boundaries). Despite diverse site-specific factors, we find widespread evidence of significantly differing rates of intensification for mean and median global average measures of PM and SM intensification, with global $P_{A,SM} \approx 0.65P_{A,PM}$ and $P_{E,SM} \approx 0.55P_{E,PM}$. Given greater PM geographic consistency (Figure 3), longer-range PM multi-teleconnections (Figures 10 and 11), and the inherent quasi-linear nature of the PM source, we consider mechanisms by which observed SM intensity could lag PM intensity in a generally widely intensifying global wind and wave climate (Reguero et al., 2019; Young & Ribal, 2019).

As noted in Section 3.1, Class II (coastal reflection) SM source contributions should correlate best with same-station PM intensity since coastal reflections and their causative incoming swell both traverse near-coastal PM-band source zones. SM amplitudes also show significantly larger observed coefficients of variation compared to contemporaneous PM amplitudes due to the nonlinearity of the SM source process (Section 3.1). An

increase in coefficient of variation due to general wave state intensification will result in greater SM trend error bounds, as observed (Figure S7 in Supporting Information S1, and Figure 7) but will not create SM trend bias relative to the PM. Because the Class II SM source process is most dependent on fixed geographical and geological controls, we suggest that differences in global average PM and SM trends do not reflect a systematic secular change in Class II wave state, but arise from other components of the SM source process.

Class I and III SM sources can generate highly uncorrelated PM-energy in ocean regions where Class II sources are small. A slower intensification in Class I and/or III compatible ocean wave-states is thus consistent with global average PM and SM trend rate differences, and could occur due to increased wave directional distribution (Class I) or from reduced energy in intra-storm or crossing wave systems (IIIa and IIIb, respectively; Ardhuin et al., 2011; Traer & Gerstoft, 2014). Additionally, energy in crossing seas might intensify at relatively higher rates in SM source regions that are poorly seismically observed, due to unfavorable ocean depth resonance and/or because they generate SM Rayleigh waves in remote ocean regions that are not consistently observed by land-based stations due to ocean-continent scattering (Bromirski et al., 2013; Le Pape et al., 2021; Tanimoto & Anderson, 2023).

With the above points in mind, we offer three nonexclusive wave state hypotheses that would diminish the intensification rate of the global SM relative to the global PM: (a) Increasing directional incoherence (reduction of observed Class I interactions); (b) changes in storm tracks that increase crossing sea amplitudes more slowly in observable SM source regions while increasing them more rapidly in poorly seismically observed regions (relatively slower intensification of observed Class III sources); and (c) Increasing swell unidirectionality (reduction of observed Class III sources). These hypotheses should be testable for recent data via improved PM and SM (perhaps including body and Love waves) global source and seismic intensity modeling and source location (e.g., Gerstoft et al., 2008; Igel et al., 2023; Landes et al., 2010) constrained by wave hindcast estimates and, at longer periods, by improving period-dependent high resolution observations of crossing and unidirectional sea state (e.g., Ardhuin et al., 2025a; Bohé et al., 2025). Consistent wave state estimation and seismic modeling for recent data would then allow for more confident interpretation of older data and improved understanding of decades of uniform and period-dependent microseism records. We suggest that increasing ocean wave unidirectionality (hypothesis c) is a simple hypothesis for global lower SM intensification relative to PM intensification. This hypothosis is also consistent with long period PM intensification (Figure 16) driven by a small increase in large-fetch storms that increase unidirectional global wave state components more rapidly than crossing seas.

4. Conclusions

We find widespread global evidence of secular intensification in both primary (PM; 14–20 s) and secondary microseism (SM; 4–10 s) amplitudes. Results include 3σ-significant positive secular rates of increase at 61 (84%) and 46 (63%) of stations for the PM and SM microseism bands, respectively, and 3σ-significant global average intensification is apparent in all eight 2 s bands between 4 and 20 s except for 6–8 s (where the confidence was 2σ). PM and SM band secular trends are appreciably correlated at seismic station sites. The globally averaged SM rate of secular amplitude change being about 0.65 times that of the PM, with global average rates of 0.17 ± 0.04%/yr and 0.11 ± 0.05%/yr, for the PM and SM respectively, with corresponding rates of energy increase of 0.27 ± 0.08 and 0.15 ± 0.09%/yr. Six stations in the Northern and Western Pacific region (8%) comprise the sole station population with jointly negative PM and SM trends at 3σ confidence.

Multiyear interstation microseism amplitude time series correlations display systematic distance and period dependencies. PM band time series display much higher inter-period correlations, and correlate over substantially greater interstation distances than SM band amplitudes. The longest PM periods, approaching 20 s, show significant interstation correlations to antipodal distances, reaffirming the suitability of PM metrics as proxies for large-scale and long-term near-coastal swell-band wave state. Conversly, much greater variability in SM inter-band and interstation correlations reflect greater sensitivity to regional wave state and the nonlinear and more period-dependent SM source process.

Three reinforcing teleconnections contribute to extensive interstation geographic correlations in microseism amplitude time series, most evident the PM period band. First, the generation of long-period swell by extensive directional surface ocean wind fields (Gjevik et al., 1988; WAM Group, 1988) from large storms creates large-scale geographically correlated excitation in PM (near-coastal) source zones (Gualtieri et al., 2019). Second, Rayleigh waves in the microseism band propagate to large distances with little attenuation (Hearn, 2024; Ma et al., 2015; Park et al., 2005), particularly for continent-crossing paths and at longer PM periods. Third, long-

range geographic wave state correlations are enhanced by inter-basin, tropical-extratropical-subtropical, and inter-hemispheric storm activity atmospheric teleconnections, including those driven by ENSO excursions that appear in global average microseism intensity histories (Aster et al., 2023; Liu et al., 2024; Odériz et al., 2021).

SM amplitudes exhibit larger time series coefficients of variation relative to PM amplitudes, consistent with a model of power law scaling of PM-correlated SM amplitude and with (non-linear) SM source theory. Also consistent with widespread power law scaling, SM to PM coefficients-of-variation ratios scale asymptotically with SM to PM log-signal correlation at most stations. Exceptions to SM to PM power law scaling occur at some ocean islands, in continental Antarctica (where microseism intensity is strongly affected by seasonal sea ice), and for an unusual site cluster in East Asia reflecting unique microseism source conditions in the South and East China Seas. There is a widespread dichotomy of SM versus PM amplitude behavior between the Northern and Southern hemispheres. This is characterized by lower SM to PM Southern Hemisphere amplitude correlations, consistent with the lessened influence of coastal reflection SM sources in the more ocean-dominated Southern Hemisphere. Conversely, there is a high incidence of quasi-quadratic SM versus PM scaling and high SM to PM correlation at North American, Western Eurasian, and Northern Australian sites where coastal reflection of PM-causative swell and consequent crossing sea conditions provide strong contributions to regional SM generation.

Lower SM intensification rates compared to the PM may reflect relatively lower rates of intensification in the deep-water broad wave directional spectrum (Class I), or in the intra- (Class IIIa) or inter-storm (Class IIIb) components of SM-causative wave state (Ardhuin et al., 2011), such as could arise from increasing unidirectionality in global ocean wave state at swell periods.

Consistent with an increasing unidirectionality hypothesis, we note increasing bi-hemispherical global average rates of PM secular intensification with increasing period consistent with a broadening of the longest-period swell spectrum on the order of 0.01%/yr. Such a spectral change could reflect an increasing rate of larger storms that support extensive fetch zones and higher wind speeds.

The 730 multi-decade time series analyzed in this study affirm that the seismic record of ocean climate is rich in period-dependent wave-state information. Consistent growth in the density and geographic distribution of broadband seismic stations, in international federated data systems, and continued innovation in seismic methodologies will steadily improve this resource with time. This includes rapidly developing undersea fiber optic and augmented ocean cable instrumentation capabilities that hold promise for revolutionary improvements in seismic and pressure sensing in the near-coastal and deep oceans (e.g., Howe et al., 2019; Liu et al., 2025; Yang et al., 2025).

Understanding of current and past wave state will benefit from improved seismic data assimilation with complementary wave state data and data products. This requires further improvements in PM and SM microseism source location and period-dependent waveform and intensity modeling. Such seismic modeling capabilities will improve the testing of hypotheses for changing period-dependent wave state, enhance understanding of secular change, and facilitate increasing use of seismic data in near-real time and historic wave state assessments integrated with other ocean wave state resources.

Conflict of Interest

The authors declare no conflicts of interest relevant to this study.

Availability Statement

Data examined and used in this work are freely available from the EarthScope Data Management Center at https://www.earthscope.org/data under network codes AS (Albuquerque Seismological Laboratory (ASL)/USGS, 1976), CU (Albuquerque Seismological Laboratory (ASL)/USGS, 2006), DW (Albuquerque Seismological Laboratory (ASL)/USGS, 1980), G (Institut De Physique Du Globe De Paris (IPGP) & Ecole Et Observatoire Des Sciences De La Terre De Strasbourg (EOST), 1982), IC (Albuquerque Seismological Laboratory (ASL)/USGS, 1992), II (Scripps Institution of Oceanography, 1986), and IU (Albuquerque Seismological Laboratory (ASL)/USGS, 1988). Data processing, analysis and plotting were performed using MATLAB© version R2024b and the ObsPy Python package (Beyreuther et al., 2010). WAVEWATCH III hindcast information, data, and products are accessible from NOAA/NCEP at https://polar.ncep.noaa.gov/waves/ensemble. All

code used for analysis will be made freely available at the time of publication at https://code.usgs.gov/asl/papers/ringler. Any use of trade, firm, or product names is for descriptive purposes only and does not imply endorsement by the US government.

Acknowledgments
This work was supported by NSF awards 2422648 and 2422649. RCA received support during 2024–2025 through the Princeton University Harry H. Hess Distinguished Visiting Faculty and the California Institute of Technology Moore Distinguished Scholars programs. Jason Becker provided data and software assistance during the final revision of this manuscript. We thank Will Yeck and two anonymous reviewers for their valuable reviews that improved this manuscript. The facilities of the EarthScope Consortium were used to access seismic waveforms, related metadata, and/or derived products through the US National Science Foundation Seismological Facility for the Advancement of Geoscience (SAGE) Award under Cooperative Agreement EAR-1724509. The Global Seismographic Network (GSN) is a cooperative scientific facility operated jointly by the National Science Foundation (NSF) and the U.S. Geological Survey (USGS). The NSF component is part of the NSF SAGE Facility, operated by the EarthScope Consortium under Cooperative Agreement EAR-1724509.

References

Albeck-Ripka, L. (2023). Waves along California's Coast are getting bigger, study says [News Article]. www.nytimes.com/2023/08/28/climate/waves-california-climate-change.html

Albuquerque Seismological Laboratory (ASL)/USGS. (1988). Global Seismograph Network—IRIS/USGS [Dataset]. *International Federation of Digital Seismograph Networks*. https://doi.org/10.7914/SN/IU

Albuquerque Seismological Laboratory (ASL)/USGS. (1976). Modified high gain long period observatory [Dataset]. *International Federation of Digital Seismograph Networks*. https://doi.org/10.7914/SN/AS

Albuquerque Seismological Laboratory (ASL)/USGS. (1980). Digital World-Wide Standardized Seismograph Network [Dataset]. *International Federation of Digital Seismograph Networks*. https://doi.org/10.7914/SN/DW

Albuquerque Seismological Laboratory (ASL)/USGS. (1992). New China Digital Seismograph Network [Dataset]. *International Federation of Digital Seismograph Networks*. https://doi.org/10.7914/SN/IC

Albuquerque Seismological Laboratory (ASL)/USGS. (2006). Caribbean USGS Network [Dataset]. *International Federation of Digital Seismograph Networks*. https://doi.org/10.7914/SN/CU

Anderson, D., Anderson, J., Ford, D., Gee, L. S., Gyure, G., Hutt, C. R., et al. (2015). Upgrade of the new China Digital Seismograph Network. *Seismological Research Letters*, *86*(5), 1364–1373. https://doi.org/10.1785/0220140182

Anthony, R., Aster, R. C., & McGrath, D. (2017). Links between atmosphere, ocean, and cryosphere from two decades of microseism observations on the Antarctic Peninsula. *Journal of Geophysical Research. Earth Surface*, *121*(1), 153–166. https://doi.org/10.1002/2016JF004098

Ardhuin, F. (2018). Large-scale forces under surface gravity waves at a wavy bottom: A mechanism for the generation of primary microseisms. *Geophysical Research Letters*, *45*(16), 8173–8181. https://doi.org/10.1029/2018GL078855

Ardhuin, F., Gualtieri, L., & Stutzmann, E. (2015). How ocean waves rock the Earth: Two mechanisms explain microseisms with periods 3 to 300 s. *Geophysical Research Letters*, *42*(3), 765–772. https://doi.org/10.1002/2014GL062782

Ardhuin, F., Postec, T., Accensi, M., Piolle, J. F., Dodet, G., Passaro, M., et al. (2025). Sizing the largest ocean waves using the SWOT mission. *Proceedings of the National Academy of Sciences of the U S A*, *122*(38), e2513381122. https://doi.org/10.1073/pnas.2513381122

Ardhuin, F., Stopa, J. E., Chapron, B., Collard, F., Husson, R., Jensen, R. E., et al. (2019). Observing sea states. *Frontiers in Marine Science*, *6*, 124. https://doi.org/10.3389/fmars.2019.00124

Ardhuin, F., Stutzmann, E., Schimmel, M., & Mangeney, A. (2011). Ocean wave sources of seismic noise. *Journal of Geophysical Research*, *116*(C9), C09004. https://doi.org/10.1029/2011JC006952

Arya, L., Hung, S., Reddy, R., Kuo, B., Lin, C., Lin, P. P., et al. (2025). Microseisms and their relationship with solid Earth, ocean, and atmospheric dynamics: Insights from ocean bottom seismometer observations in the Northern Okinawa trough-Ryukyu Arc-Trench system. *Journal of Geophysical Research: Solid Earth*, *130*(12), e2024JB031060. https://doi.org/10.1029/2024jb031060

Aster, R. C., McNamara, D. E., & Bromirski, P. D. (2008). Multidecadal climate-induced variability in microseisms. *Seismological Research Letters*, *79*(2), 194–202. https://doi.org/10.1785/gssrl.79.2.194

Aster, R. C., McNamara, D. E., & Bromirski, P. D. (2010). Global trends in extremal microseism intensity. *Geophysical Research Letters*, *37*(14), L14303. https://doi.org/10.1029/2010gl043472

Aster, R. C., Ringler, A. T., Anthony, R. E., & Lee, T. A. (2023). Increasing ocean wave energy observed in Earth's seismic wavefield since the late 20th century. *Nature Communications*, *14*(1), 6984. https://doi.org/10.1038/s41467-023-42673-w

Baker, M. G., & Abbott, R. E. (2022). Rapid refreezing of a marginal ice zone across a seafloor distributed acoustic sensor. *Geophysical Research Letters*, *49*(24), e2022GL099880. https://doi.org/10.1029/2022gl099880

Barnard, P. L., Short, A. D., Harley, M. D., Splinter, K. D., Vitousek, S., Turner, I. L., et al. (2015). Coastal vulnerability across the Pacific dominated by El Niño/Southern Oscillation. *Nature Geoscience*, *8*(10), 801–807. https://doi.org/10.1038/ngeo2539

Beyreuther, M., Barsch, R., Krischer, L., Megies, T., Behr, Y., & Wassermann, J. (2010). ObsPy: A python toolbox for seismology [Software]. *Seismological Research Letters*, *81*(3), 530–533. https://doi.org/10.1785/gssrl.81.3.530

Bohé, A., Chen, A., Chen, C., Dubois, P., Fore, A., Molero, B., et al. (2025). Measuring significant wave height fields in two dimensions at kilometric scales with SWOT. *IEEE Transactions on Geoscience and Remote Sensing*, *63*, 1–19. https://doi.org/10.1109/tgrs.2025.3551605

Borzì, A. M., Cannata, A., Panzera, F., D'Amico, S., Lo Re, C., & Aster, R. C. (2025). Microseism amplitude and wave power in the Mediterranean Sea (1996–2023). *Journal of Geophysical Research: Solid Earth*, *130*(1), e2024JB030528. https://doi.org/10.1029/2024JB030528

Borzi, A. M., Minio, V., Cannavo, F., Cavallaro, A., D'Amico, S., Gauci, A., et al. (2022). Monitoring extreme meteo-marine events in the Mediterranean area using the microseism (Medicane Apollo case study). *Scientific Reports*, *12*(1), 21363. https://doi.org/10.1038/s41598-022-25395-9

Bromirski, P. D. (2001). Vibrations from the "Perfect Storm". *Geochemistry, Geophysics, Geosystems*, *2*(7), 2000GC000119. https://doi.org/10.1029/2000GC000119

Bromirski, P. D. (2023). Climate-induced decadal ocean wave height variability from microseisms: 1931–2021. *Journal of Geophysical Research. Oceans*, *128*(8), e2023JC019722. https://doi.org/10.1029/2023JC019722

Bromirski, P. D., Cayan, D. R., Helly, J., & Wittmann, P. (2013). Wave power variability and trends across the North Pacific. *Journal of Geophysical Research. Oceans*, *118*(12), 1–20. https://doi.org/10.1002/2013JC009189

Bromirski, P. D., Flick, R. E., & Graham, N. (1999). Ocean wave height determined from inland seismometer data: Implications for investigating wave climate changes in the NE Pacific. *Journal of Geophysical Research. Oceans*, *104*(C9), 20753–20766. https://doi.org/10.1029/1999JC900156

Cannata, A., Cannavo, F., Moschella, S., Gresta, S., & Spina, L. (2019). Exploring the link between microseism and sea ice in Antarctica by using machine learning. *Scientific Reports*, *9*(1), 13050. https://doi.org/10.1038/s41598-019-49586-z

Cessaro, R. K. (1994). Sources of primary and secondary microseisms. *Bulletin of the Seismological Society of America*, *84*(1), 142–148. https://doi.org/10.1785/bssa0840010142

Chen, J. F., Park, S., & MacAyeal, D. R. (2025). Tracking multiyear sea-ice variation in the Arctic Ocean over decades with microseism. *Geophysical Research Letters*, *52*(2), e2024GL111159. https://doi.org/10.1029/2024gl111159

Chen, W.-B. (2024). Analysing seven decades of global wave power trends: The impact of prolonged ocean warming. *Applied Energy*, *356*, 122440. https://doi.org/10.1016/j.apenergy.2023.122440

Cheung, H. M., & Chu, J.-E. (2023). Global increase in destructive potential of extratropical transition events in response to greenhouse warming. *npj Climate and Atmospheric Science*, *6*(1), 137. https://doi.org/10.1038/s41612-023-00470-8

Davis, P. (2024). Development and operation of a global-scale seismographic network: The IRIS/USGS GSN. *Perspectives of Earth and Space Scientists*, *5*(1), e2023CN000225. https://doi.org/10.1029/2023cn000225

Dean, R. G., & Dalrymple, R. A. (1991). *Water wave mechanics for engineers and scientists* (Vol. 2). World Scientific Publishing.

Dierssen, H. M., & Theberge, A. E. (2014). Bathymetry: Features and hypsography. In Y. Wang (Ed.), *Encyclopedia of natural resources, volume II — Water and air (chap. 7)*. CRC Press. https://doi.org/10.1081/E-ENRW-120048589

Earlie, C. S., Young, A. P., Masselink, G., & Russell, P. E. (2015). Coastal cliff ground motions and response to extreme storm waves. *Geophysical Research Letters*, *42*(3), 847–854. https://doi.org/10.1002/2014gl062534

Ebeling, C. W., & Stein, S. (2011). Seismological identification and characterization of a large hurricane. *Bulletin of the Seismological Society of America*, *101*(1), 399–403. https://doi.org/10.1785/0120100175

Erikson, L., Morim, J., Hemer, M., Young, I., Wang, X. L., Mentaschi, L., et al. (2022). Global ocean wave fields show consistent regional trends between 1980 and 2014 in a multi-product ensemble. *Communications Earth & Environment*, *3*(1), 320. https://doi.org/10.1038/s43247-022-00654-9

Gal, M., Reading, A. M., & Ellingsen, S. P. (2019). Short timescale analysis of microseisms and application to array calibration. *Journal of Geophysical Research: Solid Earth*, *124*(3), 2684–2701. https://doi.org/10.1029/2018jb016959

Gerstoft, P., Shearer, P. M., Harmon, N., & Zhang, J. (2008). Global P, PP, and PKP wave microseisms observed from distant storms. *Geophysical Research Letters*, *35*(23). https://doi.org/10.1029/2008gl036111

Gerstoft, P., & Tanimoto, T. (2007). A year of microseisms in Southern California. *Geophysical Research Letters*, *34*(20). https://doi.org/10.1029/2007gl031091

Gjevik, B., Rygg, O., Krogstad, H., & Lygre, A. (1988). Long period swell wave events on the Norwegian shelf. *Journal of Physical Oceanography*, *18*(5). https://doi.org/10.1175/1520-0485(1988)018⟨0724:LPSWEO⟩2.0.CO;2

Grevemeyer, I., Herber, R., & Essen, H. H. (2000). Microseismological evidence for a changing wave climate in the Northeast Atlantic Ocean. *Nature*, *408*(6810), 349–352. https://doi.org/10.1038/35042558

Grob, M., Maggi, A., & Stutzmann, E. (2011). Observations of the seasonality of the Antarctic microseismic signal, and its association to sea ice variability. *Geophysical Research Letters*, *38*(11), L11302. https://doi.org/10.1029/2011GL047525

Gualtieri, L., Stutzmann, E., Juretzek, C., Hadziioannou, C., & Ardhuin, F. (2019). Global scale analysis and modelling of primary microseisms. *Geophysical Journal International*, *218*(1), 560–572. https://doi.org/10.1093/gji/ggz161

Gutenberg, B. (1947). Microseisms and weather forecasting. *Journal of the Atmospheric Sciences*, *4*(1), 21–28. https://doi.org/10.1175/1520-0469(1947)004⟨0021:MAWF⟩2.0.CO;2

Hasselmann, K. (1963). A statistical analysis of the generation of microseisms. *Reviews of Geophysics*, *1*(2), 177–210. https://doi.org/10.1029/RG001i002p00177

Hearn, T. M. (2024). Global Rayleigh wave attenuation and group velocity from International Seismological Centre data. *Geosciences*, *14*(2), 50. https://doi.org/10.3390/geosciences14020050

Howe, B. M., Arbic, B. K., Aucan, J., Barnes, C. R., Bayliff, N., Becker, N., et al. (2019). SMART cables for observing the global ocean: Science and implementation. *Frontiers in Marine Science*, *6*, 424. https://doi.org/10.3389/fmars.2019.00424

Igel, J. K. H., Bowden, D. C., & Fichtner, A. (2023). SANS: Publicly available daily multi-scale seismic ambient noise source maps. *Journal of Geophysical Research: Solid Earth*, *128*(1), e2022JB025114. https://doi.org/10.1029/2022JB025114

Igel, J. K. H., Ermert, L. A., & Fichtner, A. (2021). Rapid finite-frequency microseismic noise source inversion at regional to global scales. *Geophysical Journal International*, *227*(1), 169–183. https://doi.org/10.1093/gji/ggab210

Institute De Physique Du Globe De Paris (IPGP)Ecole Et Observatoire Des Sciences De La Terre De Strasbourg (EOST). (1982). GEOSCOPE, French global network of broad band seismic stations [Dataset]. *Institute De Physique Du Globe De Paris (IPGP)*. https://doi.org/10.18715/GEOSCOPE.G

John, S., & West, M. E. (2025). Storms, sea ice, and microseismic noise in Alaska. *Journal of Geophysical Research: Solid Earth*, *130*(4), e2024JB030603. https://doi.org/10.1029/2024jb030603

Kedar, S. (2011). Source distribution of ocean microseisms and implications for time-dependent noise tomography. *Comptes Rendus Geoscience*, *343*(8–9), 548–557. https://doi.org/10.1016/j.crte.2011.04.005

Kedar, S., Longuet-Higgins, M., Webb, F., Graham, N., Clayton, R., & Jones, C. (2008). The origin of deep ocean microseisms in the North Atlantic Ocean. *Proceedings of the Royal Society a-Mathematical Physical and Engineering Sciences*, *464*(2091), 777–793. https://doi.org/10.1098/Rspa.2007.0277

Kedar, S., & Webb, F. H. (2005). The ocean's seismic hum. *Science*, *307*(5710), 682–683. https://doi.org/10.1126/science.1108380

Landes, M., Hubans, F., Shapiro, N. M., Paul, A., & Campillo, M. (2010). Origin of deep ocean microseisms by using teleseismic body waves. *Journal of Geophysical Research: Solid Earth*, *115*(B5), B05302. https://doi.org/10.1029/2009jb006918

Lecocq, T., Hicks, S. P., Noten, K. V., van Wijk, K., Koelemeijer, P., Plaen, R. S. M. D., et al. (2020). Global quieting of high-frequency seismic noise due to COVID-19 pandemic lockdown measures. *Science*, *369*(6509), 1338–1343. https://doi.org/10.1126/science.abd2438

Lee, T. A., Ishii, M., & Okubo, P. (2020). Relative time corrections for historical analog seismograms using the single-day ambient noise correlation function. *Bulletin of the Seismological Society of America*, *110*(6), 3185–3195. https://doi.org/10.1785/0120190313

Lee, T. A., Ringler, A. T., Anthony, R. E., & Ishii, M. (2023). Comparison of corecorded analog and digital systems for characterization of responses and uncertainties. *Seismological Research Letters*, *94*(5), 2301–2312. https://doi.org/10.1785/0220230129

Le Pape, F., Craig, D., & Bean, C. J. (2021). How deep ocean-land coupling controls the generation of secondary microseism Love waves. *Nature Communications*, *12*(1), 2332. https://doi.org/10.1038/s41467-021-22591-5

Leroy, N., Vallée, M., Zigone, D., Romanowicz, B., Stutzmann, E., Maggi, A., et al. (2023). GEOSCOPE Network: 40 yr of global broadband seismic data. *Seismological Research Letters*, *95*(3), 1495–1517. https://doi.org/10.1785/0220230176

Li, L., Boué, P., Retailleau, L., & Campillo, M. (2020). Spatiotemporal correlation analysis of noise-derived seismic body waves with ocean wave climate and microseism sources. *Geochemistry, Geophysics, Geosystems*, *21*(9), e2020GC009112. https://doi.org/10.1029/2020gc009112

Lighthill, J. (1996). *Waves in fluids*. Cambridge University Press.

Lin, F.-C., Ritzwoller, M. H., & Shapiro, N. M. (2006). Is ambient noise tomography across ocean basins possible? *Geophysical Research Letters*, *33*(14). https://doi.org/10.1029/2006gl026610

Liu, J., Li, R., Li, S., Meucci, A., & Young, I. R. (2024). Increasing wave power due to global climate change and intensification of Antarctic oscillation. *Applied Energy*, *358*, 122572. https://doi.org/10.1016/j.apenergy.2023.122572

Liu, M., Costa, L., Mertz, P., Varughese, S., Edirisinghe, S., Kamalov, V., & Zhan, Z. (2025). Trans-oceanic distributed sensing of tides over telecommunication cable between Portugal and Brazil. *Geophysical Research Letters*, *52*(12), e2024GL114414. https://doi.org/10.1029/2024gl114414

Longuet-Higgins, M. (1950). A theory of the origin of microseisms. *Philosophical Transactions of the Royal Society of London. Series A, Mathematical and Physical Sciences*, *243*(857), 1–35. https://doi.org/10.1098/rsta.1950.0012

Ma, Z., Masters, G., & Mancinelli, N. (2015). Two-dimensional global Rayleigh wave attenuation model by accounting for finite-frequency focusing and defocusing effect. *Geophysical Journal International*, *204*(1), 631–649. https://doi.org/10.1093/gji/ggv480

Markovitz, E., & Steiger, N. J. (2025). Contemporary megadrought on Easter Island (Rapa Nui) since 2010. *Geophysical Research Letters*, *52*(21), e2025GL115880. https://doi.org/10.1029/2025gl115880

Meucci, A., Young, I. R., Pepler, A., Rudeva, I., Ribal, A., Bidlot, J., & Babanin, A. V. (2023). Evaluation of spectral wave models physics as applied to a 100-year Southern Hemisphere extra-tropical cyclone sea state. *Journal of Geophysical Research. Oceans*, *128*(9), e2023JC019751. https://doi.org/10.1029/2023jc019751

Michaelis, A. C., Willison, J., Lackmann, G. M., & Robinson, W. A. (2017). Changes in winter north Atlantic extratropical cyclones in high-resolution regional pseudo–global warming simulations. *Journal of Climate*, *30*(17), 6905–6925. https://doi.org/10.1175/jcli-d-16-0697.1

Minio, V., Borzì, A. M., Saitta, S., Alparone, S., Cannata, A., Ciraolo, G., et al. (2023). Towards a monitoring system of the sea state based on microseism and machine learning. *Environmental Modelling & Software*, *167*, 105781. https://doi.org/10.1016/j.envsoft.2023.105781

Nakata, N., Gualtieri, L., & Fichtner, A. (2019). *Seismic ambient noise*. Cambridge University Press.

Nawa, K., Suda, N., Fukao, Y., Sato, T., Aoyama, Y., & Shibuya, K. (1998). Incessant excitation of the Earth's free oscillations. *Earth Planets and Space*, *50*(1), 3–8. https://doi.org/10.1186/BF03352080

Niklasson, S., Rowe, C., & Bilek, S. (2025). Seafloor seismic noise patterns across the Pacific basin. *Seismological Research Letters*, *96*(2A), 772–783. https://doi.org/10.1785/0220240361

Nishida, K. (2017). Ambient seismic wave field. *Proceedings of the Japan Academy. Series B, Physical and Biological Sciences*, *93*(7), 423–448. https://doi.org/10.2183/pjab.93.026

Nishida, K., Kawakatsu, H., Fukao, Y., & Obara, K. (2008). Background Love and Rayleigh waves simultaneously generated at the Pacific Ocean floors. *Geophysical Research Letters*, *35*(16). https://doi.org/10.1029/2008gl034753

Odériz, I., Silva, R., Mortlock, T. R., Mori, N., Shimura, T., Webb, A., et al. (2021). Natural variability and warming signals in global ocean wave climates. *Geophysical Research Letters*, *48*(11), e2021GL093622. https://doi.org/10.1029/2021gl093622

Omori, F. (1901). *Publications in foreign languages* (Vol. 5). Japanese Earthquake Investigation Committee.

Park, J., Anderson, K., Aster, R., Butler, R., Lay, T., & Simpson, D. (2005). Global seismographic network records the great Sumatra-Andaman earthquake. *EOS, Transactions of the American Geophysical Union*, *86*(6), 57–64. https://doi.org/10.1029/2005eo060001

Peterson, J. (1993). *Observations and modeling of seismic background noise* (Vol. 93–322, p. 94). U.S. Geological Survey Open-File Report.

Pratt, M. J., Wiens, D. A., Winberry, J. P., Anandakrishnan, S., & Euler, G. G. (2017). Implications of sea ice on Southern Ocean microseisms detected by a seismic array in West Antarctica. *Geophysical Journal International*, *209*, 492–507. https://doi.org/10.1093/gji/ggx007

Priestley, M. D. K., & Catto, J. L. (2022). Future changes in the extratropical storm tracks and cyclone intensity, wind speed, and structure. *Weather and Climate Dynamics*, *3*(1), 337–360. https://doi.org/10.5194/wcd-3-337-2022

Reguero, B. G., Losada, I. J., & Méndez, F. J. (2019). A recent increase in global wave power as a consequence of oceanic warming. *Nature Communications*, *10*(1), 205. https://doi.org/10.1038/s41467-018-08066-0

Ringler, A. T., Anthony, R. E., Aster, R. C., Ammon, C. J., Arrowsmith, S., Benz, H., et al. (2022). Achievements and prospects of global broadband seismographic networks after 30 years of continuous geophysical observations. *Reviews of Geophysics*, *60*(3), e2021RG000749. https://doi.org/10.1029/2021rg000749

Ringler, A. T., Storm, T., Gee, L. S., Hutt, C. R., & Wilson, D. (2014). Uncertainty estimates in broadband seismometer sensitivities using microseisms. *Journal of Seismology*, *19*(2), 317–327. https://doi.org/10.1007/s10950-014-9467-7

Ringler, A. T., Wilson, D. C., Wolin, E., Storm, T., & Sandoval, L. (2019). Calibration analysis and noise estimates of WWSSN station ALQ (Albuquerque, New Mexico). *Seismological Research Letters*, *91*(3), 1359–1366. https://doi.org/10.1785/0220190201

Sasaki, W. (2014). Changes in the North Pacific wave climate since the mid-1990s. *Geophysical Research Letters*, *41*(22), 7854–7860. https://doi.org/10.1002/2014gl061590

Scripps Institution of Oceanography. (1986). Global Seismograph Network—IRIS/IDA [Dataset]. *International Federation of Digital Seismograph Networks*. https://doi.org/10.7914/SN/II

Sergeant, A., Stutzmann, E., Maggi, A., Schimmel, M., Ardhuin, F., & Obrebski, M. (2013). Frequency-dependent noise sources in the North Atlantic Ocean. *Geochemistry, Geophysics, Geosystems*, *14*(12), 5341–5353. https://doi.org/10.1002/2013gc004905

Shabtian, H. S., Eilon, Z. C., & Tanimoto, T. (2023). Seasonality of California central coast microseisms. *Bulletin of the Seismological Society of America*, *114*(2), 873–881. https://doi.org/10.1785/0120230201

Shaffrey, L. C., Zappa, G., Hodges, K. I., Sansom, P. G., & Stephenson, D. B. (2013). A multimodel assessment of future projections of North Atlantic and European extratropical cyclones in the CMIP5 climate models. *Journal of Climate*, *26*(16), 5846–5862. https://doi.org/10.1175/jcli-d-12-00573.1

Shapiro, N. M., & Campillo, M. (2004). Emergence of broadband Rayleigh waves from correlations of the ambient seismic noise. *Geophysical Research Letters*, *31*(7). https://doi.org/10.1029/2004gl019491

Shaw, T. A., & Miyawaki, O. (2023). Fast upper-level jet stream winds get faster under climate change. *Nature Climate Change*, *14*(1), 61–67. https://doi.org/10.1038/s41558-023-01884-1

Stutzmann, E., Schimmel, M., Patau, G., & Maggi, A. (2009). Global climate imprint on seismic noise. *Geochemistry, Geophysics, Geosystems*, *10*(11). https://doi.org/10.1029/2009gc002619

Tanimoto, T., & Anderson, A. (2023). Seismic noise between 0.003 Hz and 1.0 Hz and its classification. *Progress in Earth and Planetary Science*, *10*(1), 56. https://doi.org/10.1186/s40645-023-00587-7

Tian, Y., & Ritzwoller, M. H. (2015). Directionality of ambient noise on the Juan de Fuca plate: Implications for source locations of the primary and secondary microseisms. *Geophysical Journal International*, *201*(1), 429–443. https://doi.org/10.1093/gji/ggv024

Traer, J., & Gerstoft, P. (2014). A unified theory of microseisms and hum. *Journal of Geophysical Research: Solid Earth*, *119*(4), 3317–3339. https://doi.org/10.1002/2013jb010504

Traer, J., Gerstoft, P., Bromirski, P. D., & Shearer, P. (2012). Microseisms and hum from ocean surface gravity waves. *Journal of Geophysical Research*, *117*(B11307), L13303. https://doi.org/10.1029/2012JB009550

Tsai, V. C., & McNamara, D. (2011). Quantifying the influence of sea ice on ocean microseism using observations from the Bering Sea, Alaska. *Geophysical Research Letters*, *38*(22), L22502. https://doi.org/10.1029/2011GL049791

Ulbrich, U., Leckebusch, G. C., & Pinto, J. G. (2009). Extra-tropical cyclones in the present and future climate: A review. *Theoretical and Applied Climatology*, *96*(1–2), 117–131. https://doi.org/10.1007/s00704-008-0083-8

USGS. (2017). Advanced national seismic system (ANSS) comprehensive catalog of earthquake events and products. *U.S. Geological Survey Earthquake Hazards Program*. https://doi.org/10.5066/F7MS3QZH

WAM Group. (1988). The WAM model—A third generation ocean wave prediction model. *Journal of Physical Oceanography*, *18*(12).

WAVEWATCH Center. (2019). *User manual and system documentation of WAVEWATCH III R version 6.07* (Vol. 333). NOAA/NWS/NCEP/MMAB Technical Note.

Webb, S. C. (2008). The Earth's hum: The excitation of Earth normal modes by ocean waves. *Geophysical Journal International*, *174*(2), 542–566. https://doi.org/10.1111/J.1365-246x.2008.03801.X

Xiao, H., Xue, M., Yang, T., Liu, C., Hua, Q., Xia, S., et al. (2018). The characteristics of microseisms in South China Sea: Results from a combined data set of OBSs, broadband land seismic stations, and a global wave height model. *Journal of Geophysical Research: Solid Earth*, *123*(5), 3923–3942. https://doi.org/10.1029/2017jb015291

Yang, X., Yang, J., Luo, Y., Lin, J., Liu, X., Lei, J., et al. (2025). Ocean observations using distributed acoustic sensing with a 29-km long submarine cable in the Northern South China Sea. *Seismological Research Letters*, *96*(6), 3891–3903. https://doi.org/10.1785/0220250007

Young, I., & Ribal, A. (2019). Multiplatform evaluation of global trends in wind speed and wave height. *Science*, *364*(6440), 548–552. https://doi.org/10.1126/science.aav9527

Young, I., Ziegeer, S., & Babanin, A. (2011). Global trends in wind speed and wave height. *Science*, *332*(6028), 451–455. https://doi.org/10.1126/science.1197219

Zhang, J. A., Gerstoft, P., & Bromirski, P. D. (2010). Pelagic and coastal sources of P-wave microseisms: Generation under tropical cyclones. *Geophysical Research Letters*, *37*(23), L23306. https://doi.org/10.1029/2010gl044288